Detecting Breaking Waves and Measuring Bore Speeds in Optical Surf Zone Imagery using Machine Learning

Malcolm James LeClair

A thesis
submitted in partial fulfillment of the
requirements for the degree of

Master of Science in Civil Engineering

University of Washington

2025

Committee:
Christie Hegermiller
Jim Thomson
Kara Koetje

Program Authorized to Offer Degree:
Civil and Environmental Engineering

University of Washington

Abstract

Detecting Breaking Waves and Measuring Bore Speeds in Optical Surf Zone Imagery using Machine Learning

Malcolm James LeClair

Co-Chairs of the Supervisory Committee:

Christie Hegermiller
Jim Thomson

Department of Civil and Environmental Engineering

A machine learning algorithm is developed to detect breaking waves in optical remote sensing data collected under visually diverse conditions along a kilometer-scale beach in Duck, NC. Bore speeds are estimated from the breaking-wave detections and are compared with theoretical models using surveyed bathymetry. Bathymetry inversion from the derived bore speeds is then explored, revealing low but systematic bias within the surf zone. Despite this limitation, a qualitative analysis of the inverted bathymetry demonstrates that the method captures morphological change over the course of the experiment. This method shows promise as a robust, low-cost approach for measuring wave-breaking patterns and dynamics across large surf zones. The results highlight important considerations for the data resolution, quality, and processing needed to achieve robust measurements of breaking waves using optical remote sensing.

TABLE OF CONTENTS

ACKNOWLEDGMENTS

Thank you to the DUNEX field team, especially from UW & the Field Research Facility, who collected this extensive dataset.

Chapter 1
INTRODUCTION

In the surf zone, breaking waves provide the dominant forcing for hydro- and morphodynamic processes by generating energy and momentum fluxes that drive run-up, dissipation, sediment transport, and circulation. Because wave breaking in the nearshore is predominantly depth-limited, nearshore bathymetry is a driving factor in the distribution of these fluxes and their impacts on the coastal system.

Despite its importance, the actual bathymetry of most surf zones is not accurately surveyed. Direct, in-situ surveys are time-consuming, expensive, and dangerous. Further, timescales of bathymetric variability range from decadal [68] to seasonal [16] for prominent morphologic features like sandbars (0.1–1 km) to hourly for smaller features like cusps (1–10 m) [84, 62]. This requires frequent surveys for accurate knowledge of the surf-zone bathymetry. On climatological scales, rising sea level [54] and changes in wave climate [87] are also driving long-term changes in beach morphology. Understanding these changes to beach shape and their impacts on coastal systems is essential for developing effective coastal management plans, accurate nearshore forecasts, and strategies to mitigate the long-term effects of climate change on coastal communities.

To address this need, a variety of methods have been developed to estimate nearshore bathymetry cheaply and readily from easily observed parameters. These range from simple models that invert observations of dissipation [2], wave celerity [64], wavenumber and frequency [38], and optical density [77], to complex inverse methods that [56, 92, 91, 93]. Many of these methods, such as cBathy [38], are well-established, but obtaining accurate results in the surf zone remains a challenge due to the nonlinear, nonuniform nature of breaking processes.

This thesis develops a machine-learning method for detecting breaking waves in optical video and explores its application to surf-zone bathymetry inversion. The model detects breaking waves under variable ocean, atmospheric, and optical conditions, and could, in the future, be applied to other questions of breaker dynamics in the surf zone.

First, relevant theory for describing wave breaking and speeds in the surf zone is reviewed. Prior work in remote sensing of breaking waves in shallow water and in bathymetry inversion is discussed. Then, the data and methods for detecting breaking waves, inverting their speeds, and estimating surf-zone bathymetry are presented. The accuracy of the celerity inversion method is evaluated statistically and descriptively in its ability to detect relevant nearshore features, such as alongshore variations in the location and depth of a persistent alongshore bar. Limitations of the method and considerations for remote sensing of breaking waves in the nearshore are discussed. Finally, future directions and next steps are proposed.

1.1 Nearshore and Beach Structure

A beach is an accumulation of sediment along the coastline. Its cross-shore profile, shown in Figure 1.1, is divided into several regions. The shore and upland areas include dunes and berms formed during high-energy events. Starting at the coastline, the backshore extends to the mean high water line. The foreshore reaches from the mean high water line to the mean low water line. Seaward of the water line, the profile is categorized into three main zones: the swash zone, dominated by wave run-up and backwash processes; the surf zone, where the majority of breaking occurs on the foreshore and over the bar; and the nearshore, where waves have begun shoaling but have not yet started breaking.

Nearshore bathymetry typically follows a concave shape due to the onshore transport of sediment [25]. A common deviation from this concave shape is the barred profile illustrated in Figure 1.1. Bedload convergence from the return flow and wave motions accumulates sand to form distinct troughs and bars whose presence, location, and shape vary with wave conditions. Beach shape is determined by a variety of factors, including sediment type, incident waves, water levels, and mean currents.

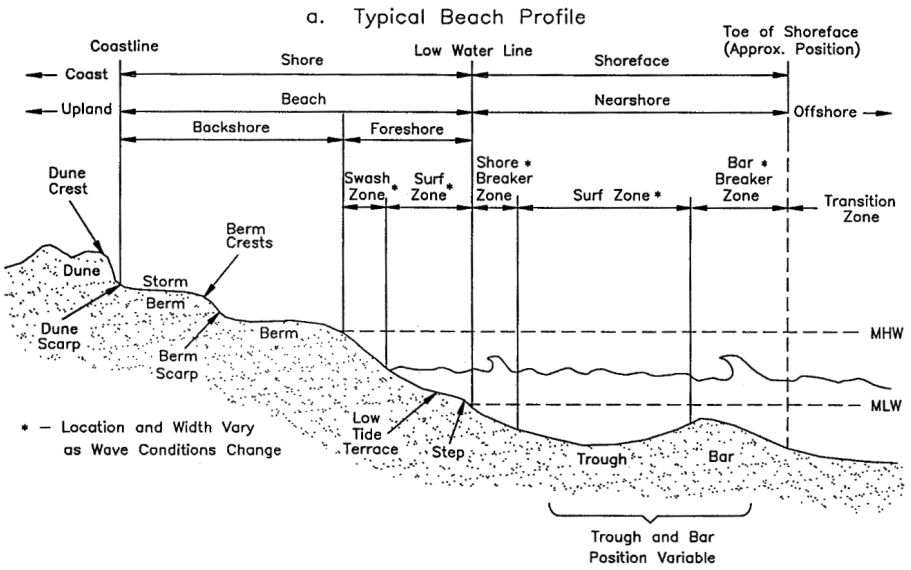

Figure 1.1: A schematic description of beach features in the nearshore. Reproduced from *Coastal Engineering Manual - Part IV-1* [57]

1.2 Surface Gravity Waves

The ocean surface is covered by wind-generated surface gravity waves with periods of roughly 1–30 s and wavelengths of 10 m to 1 km. They are referred to as short waves in contrast to tides, seiches, tsunamis, and storm surges, which have longer periods of minutes to hours. These waves are further classified into two categories: wind sea, locally generated waves with varied size and direction, and swell, remotely generated waves that have propagated some distance, and are directionally and spectrally narrower due to dispersion. Once they reach the coast, short waves are the primary drivers of sediment transport in the nearshore and play a key role in defining the beach shape [7].

1.3 Depth Limited Breaking

As surface gravity waves approach the beach and enter shallow water, they begin to experience the effects of finite depth, slowing, shoaling, and steepening. As waves steepen, they

reach kinematic and dynamic limits on their shape and break, overturning, becoming turbulent, and dissipating energy as they propagate to shore as bores. This process is known as depth-limited breaking because of its dependence on relative water depth. It is distinguished from other forms of breaking, such as whitecapping, though they may share the same physical limits [29]. In the surf zone, depth-limited breaking dominates due to the steep bathymetric gradients of the nearshore.

Several frameworks have been developed to describe and predict the onset of breaking. The first considers individual waves, for which limits on wave geometry, kinematics, and dynamics have been proposed. Geometrically, the limit is described as a function of wave steepness [55], kinematically, as a ratio of particle velocity to phase speed [8, 60, 29], and dynamically, as a limit on the rate of change of wave steepness, or local energy flux at the crest tip [61, 9]. A second framework, derived to study depth-limited breaking, reinterprets the geometry described using Stokes theory. This framework casts the steepness limit as a function of depth h, beach slope, and incident wave conditions, linking the breaking process to nearshore bathymetry.

Miche [55] used Stokes wave theory to derive a theoretical steepness limit:

$$\left[\frac{H}{L}\right]_{\max} = 0.142 \tanh(kh) \tag{1.1}$$

where H is the wave height, L is the wavelength, k is the wavenumber, and h is the water depth. This yields the classic deep water steepness limit of $\frac{H_0}{L_0} = \frac{1}{7}$, and the shallow water limit of $\frac{H_b}{h_b} = 0.88$.

Battjes [10] expands on the work of Miche to describe the heights of breaking waves H_b, as a function of k and h, by adding a free parameter γ, the breaker index. This parameter is used to empirically fit observed variations in maximum wave height for a given water depth, H_{max}/h:

$$H_b = \frac{0.88}{k} \tanh\left(\frac{\gamma}{0.88} kh\right) \tag{1.2}$$

In shallow water, this reduces to:

$$H_b = \gamma h_b \tag{1.3}$$

where the breaker index, γ, is an empirical coefficient that typically ranges from 0.3 to 1.3 depending on beach slope and incident wave steepness [10, 27, 83].

1.4 Wave Celerity

1.4.1 Non-Breaking Waves

The simplest model for a gravity wave traveling on the air-sea interface is Airy, or linear wave theory. This model is governed by the dispersion relation:

$$\omega^2 = gk \tanh(kh) \tag{1.4}$$

where ω is the frequency, g is gravity, and h is water depth. In the shallow water limit, the phase speed $c_p = \omega/k$ is given by the following, as $\tanh(kh) \approx kh$.

$$c_{p,\text{shallow}} = \sqrt{gh} \tag{1.5}$$

The limit for shallow water behavior is taken as $h < L/20$, where L is the wavelength [79].

Equation 1.5 is non-dispersive for shallow-water waves, while in practice, we expect the non-negligible amplitude of the waves to cause dispersion even in shallow water. This amplitude dispersion is represented in solitary wave theory:

$$c_{p_{\text{solitary}}} = \sqrt{g(h+H)} \tag{1.6}$$

where wave height H contributes to the effective local water depth [95].

1.4.2 Breaking Waves

These equations, derived for non-breaking waves, do not formally describe breaking waves or bores. Nonetheless, as a result of the observed similarities in particle trajectories and phase speeds between breaking and non-breaking waves [41], such models are often used to describe the propagation of breakers. For simplicity, these results are presented for waves in still water. The expected return flow down the beach under the waves would slightly decrease the phase speed [41].

Inman et al. [41], supported by observations from Thornton and Guza [82], posit that, despite the theoretical differences, the propagating bore resembles an asymmetrical solitary wave, and suggest bounds on its speed between shallow-water linear and solitary waves:

$$gh \leq c^2 \leq gh(1+\gamma) \tag{1.7}$$

Hedges [36] applies cnoidal wave theory to waves propagating in shallow water, and for convenience frames the nonlinearity as an empirical modification of the linear celerity:

$$c_{cn} = \sqrt{g(h+Z)} \tag{1.8}$$

where Z is the wave amplitude $Z = \eta; \eta \ll h$ in the small wave limit, and $Z = H$ at the solitary wave limit. Booij [17] proposes $Z = H/2$ based on data from Walker [88], later supported by Kirby and Dalrymple [42], who extended the theory to deep water.

Others have explicitly modeled the breaking wave as a propagating hydraulic jump, or bore. As described in Svendsen et al. [80], the phase speed of a propagating bore c_b can be described as:

$$\frac{c_b^2}{gh} = \frac{d_c d_t}{h^3}\frac{(d_t + d_c)}{2} \tag{1.9}$$

where d_t is the depth of the trough and d_c is the depth of the crest. In the small amplitude limit, $d_t \approx d_c \approx h$, and $c_b = \sqrt{gh}$. In the bore approximation of a solitary wave, $d_t = h,\ d_c = h + H$, the predicted speed slightly exceeds that of the solitary wave. These results similarly bound the speed to the range of Equation 1.7 [21].

A variety of nonlinear formulations for breaking wave speeds have been shown to improve celerity-based estimates of bathymetry in the surf zone [21, 51, 52].

1.5 Remote Sensing for Bathymetry Inversion

1.5.1 History of Remote Sensing Methods

Optical signatures of both breaking and non-breaking waves have been used to infer bathymetry in the presence of shoals and reefs for as long as sailors have been navigating coastal waters,

where shallow bathymetry and depth-limited breaking pose a threat to safety and navigation. During the Second World War, methods were formalized and analytically derived. They were used to estimate beach slopes while planning landings on hostile shores where charts were unavailable and direct survey was impossible.

Williams [90] details the methods developed by the British to estimate bathymetry from aerial photography. The first attempts combined photographs showing the waterline with tidal data to plot beach contours. Later methods calculated water depth using models of optical density. Finally, linear wave theory was used to estimate depth using the dispersion relation based on observations of wavelength and speed. The limited accuracy of time and position measurements with the imagery made these celerity-based methods challenging to implement. While the methods achieved usable results with errors in nearshore depth of 2–3 feet, they were particularly challenged by the presence of bars, often failing to resolve them from the mean slope.

1.5.2 Modern Tools

Technology has advanced significantly since the film photos and analog timepieces of the 1940s. The proliferation of digital photography and GPS has made accurate timestamping and georectification commonplace. Decreases in digital storage costs make it feasible and routine to capture and store large volumes of high-resolution imagery and video.

Many of the early applications of optical remote sensing in the coastal environment were from fixed towers with large systems like Argus [39], which consists of multiple cameras and data acquisition computers. These systems have been used to image the coastline and measure wave breaking, swash extent, surface currents, and morphological change.

Today, the miniaturization of digital cameras, storage, combined with the development of small Uncrewed Aerial Systems (sUAS) has made UAS-based data collection an increasingly popular low-cost and highly flexible alternative tool for remote sensing in coastal environments [40, 18, 44, 73, 49]. Commercial UAS already have the flight endurance to meet the 1024 s record standard set by the Argus system, which is needed to generate stable statistics

for observations of the surf zone. Novel technologies, like amphibious UAS that land on the water and directly sample the waves and the surface ocean, have enabled hybrid in-situ and remote sampling modalities that more comprehensively measure coastal environments [24, 30].

Increased availability and resolution of satellite imagery and video have opened the door to space-based observations of the nearshore. Several studies have explored depth estimation from satellite imagery using the dispersion relation [59, 43], machine learning [58], and color attenuation [77, 50].

1.5.3 Time Exposure Imagery

Lippmann and Holman [47] developed methods to characterize sandbar morphology using long exposures that create statistically stable images of breaker density. They assume a correlation between breaking dissipation and optical intensity based on breaker-generated bubbles and show that analytical models of breaking dissipation from Battjes and Janssen [11] and Thornton and Guza [83] produce dissipation profiles that resemble those observed in optical intensity. The presence of breaking in these images reveals sandbars and enables measurement of their width, cross-shore location, and variability, but does not provide information about their depth.

Further developing the use of optical intensity as a proxy for dissipation, Aarninkhof and Ruessink [2] and van Dongeren et al. [86] designed a method to estimate depth in the surf zone by assimilating dissipation profiles to a simple parametric model.

1.5.4 Wavenumber-Frequency Depth Inversion

Since the British work with aerial imagery in the 1940s, the linear dispersion relation has been used to relate observable parameters, such as wavelength, period, and speed, to depth. cBathy [38, 37] modernized this approach for digital imagery by estimating the wavenumber via EOF decomposition of the Fourier-domain cross-spectra of pixel intensities. The

wavenumber, k, and frequency, ω, are then used in a least-squares fit of the dispersion relation to estimate depth. Individual depth realizations are passed through a Kalman Filter to generate a time-averaged estimate, which improves performance over the tidal cycle.

Under favorable conditions, cBathy can accurately resolve nearshore bathymetry with an RMSE of 0.5 m. Performance degrades in the surf zone as the method assumes spatial homogeneity within analysis tiles. This assumption does not hold in the presence of sharp gradients, short spatial scales, and the discontinuous optical signatures of dark steepening waves and bright foam faces of breaking waves.

Other work has expanded on this ω–k approach using X-band radar [23], satellites [59], drones [40], and a variety of different processing methods, including Dynamic Mode Decomposition [71] and cross-correlation methods [63].

1.5.5 Celerity Depth Inversion

An alternative approach uses measurements of breaking and non-breaking wave speed from imagery [21, 94], pressure sensors [64], radar [12], or lidar [52], to invert for depth. Catalan and Haller [21] and Postacchini and Brocchini [64] detail the various models considered for breaker phase speed, ranging from linear waves to solitary waves and from bores to propagating shocks. These phase speed approaches still solve the dispersion relation to estimate depth. They relate phase speed, $c_p = \omega/k$, to depth through Equation 1.4. For linear waves in shallow water, the dependence on wavenumber is removed, and the phase speed becomes a direct function of depth.

1.6 Remote Sensing of Breaking Waves

Air entrainment and foam generation during wave breaking create a distinct optical signature in the visible spectrum, characterized by high diffuse reflectance and optical intensity [89]. In long exposures of the nearshore, breaking appears as white foam bands with high optical intensity. This signature has been used to measure the location and width of rips and offshore bars, and surf-zone extent [47].

1.6.1 Intensity Thresholding

One of the difficulties in connecting optical signatures to the active breaking process is the generation and advection of the persistent foam. Rising bubbles and remanent foam floating on the surface share the same bright optical signature, making them difficult to differentiate in imagery. Despite the visual similarity, this foam is not linked to the dissipation in the active breaking process.

While the optical signatures of active breaking and remanent foam are similar, RADAR returns are stronger from active breaking. Neither modality completely isolates breaking, but by fusing the two, the joint histograms can be thresholded to separate the remanent foam [22]. This technique allows segmentation on a wave-by-wave basis, enabling measurements of breaker length, area, and speed, all of which are essential parameters linking breaking to depth, dissipation, and circulation.

1.6.2 Temporal Gradients

Active breaking has a unique temporal signal that distinguishes it from the slow decay of passive foam. Aarninkhof and Ruessink [2] model the generation and decay of foam throughout its lifecycle to isolate the breaking signal from remanent foam and transient lighting effects. Aarninkhof uses this measurement of breaking as a more robust proxy for dissipation in their work on bathymetry inversion [3].

The active breaking signal, characterized by a sharp increase in intensity, stands out in timestack images, shown in Figure 1.2. This timestack shows the evolution of a cross-shore transect of 1 m^2 pixels in the vertical, at 2 Hz.

Stringari et al. [76] calculate gradients on timestack images using a Sobel filter, and set a minimum intensity gradient as the criterion for breaking. In a post-processing step, a simple neural network is used to reduce false positives by classifying detected breaking pixels as active breaking, remanent foam, or sand based on their color.

Yoo et al. [94] apply an explicit time-differencing scheme to extract the temporal breaking

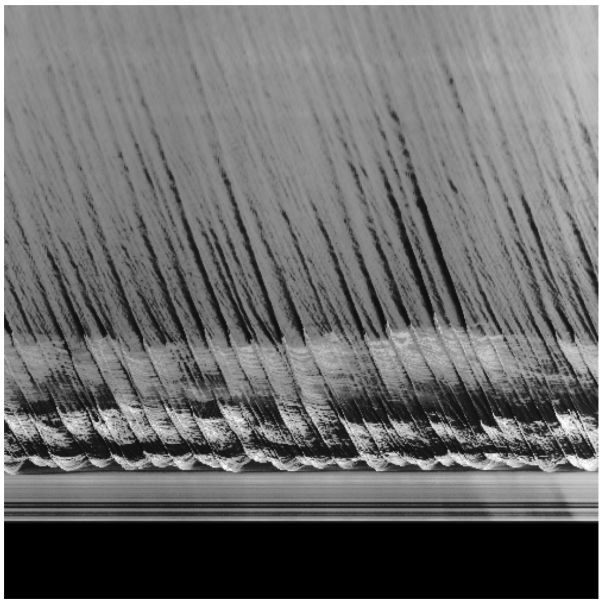

Figure 1.2: A timestack image at resolution 1 m $\times$ 0.5 s extending 500 m offshore

signal. A 2D low-pass filter then separates the dominant, large-scale breaking from sensor noise and lighting effects. Coherent breaking crests are extracted, and their speeds are estimated using the Radon transform.

These optical methods all rely on passive illumination, so they are sensitive to lighting, sky conditions, and the relative position of the sun. The best results are achieved with the high-contrast illumination of clear skies and overhead sun [76, 94, 21].

1.6.3 Machine Learning

Several machine learning approaches have been used to detect breaking waves. Identifying breaking waves in imagery is typically formulated as a semantic segmentation problem, i.e., pixel-wise classification. In this framework, the model predicts a class label for each pixel in the image, in this case, breaking or non-breaking.

This work leverages progress in machine learning for object detection and semantic seg-

mentation, which has revolutionized the field over the past decade. Today, there are numerous models and approaches to image segmentation in the computer vision field, but much of the application to breaking wave detection has been built on U-Nets [67].

Sáez et al. [81] build on earlier work detecting individual waves by Catalan et al. [22] to generate a dataset of labeled breaking waves using imagery and RADAR. The dataset is used to train a surrogate machine learning model that detects breaking from imagery alone.

Lange et al. [44] identify wave crests using a model trained on manually annotated timestacks. The wave crests are then classified as breaking or non-breaking by clustering the bimodal distribution of pixel intensities. The detections are validated using the speeds from the slope of the detected breakers to invert for depth in the surf zone. The depth estimates are accurate, and complement cBathy, improving upon its predictions where the fraction of breaking is $> 5\%$.

Others have applied machine learning to the classification of breaking waves, either to validate detections using conventional pixel-intensity threshold methods [31] or to categorize breakers as plunging, spilling, etc. [20, 66].

1.7 Limitations of Nearshore Remote Sensing

As technology has improved over the past 80 years, remote sensing has become a much more common tool for observing the nearshore. Improvements in tools and methods have made considerable strides toward demonstrating the feasibility of using remote sensing to estimate key parameters, such as depth and dissipation, in the surf zone; however, applying these methods to large, real-world datasets remains challenging. The broad range of optical signatures exhibited by breaking waves under different lighting conditions, sea states, beaches, and breaking types has so far precluded the development of a general approach to detect breaking waves. Even using machine learning, which promises robust statistics across diverse distributions, reliably detecting the optical signature of breaking waves from imagery remains an open challenge. Another fundamental limitation of many optical remote sensing methods is that they do not measure wave height. This is especially challenging in the surf

zone, where wave height is a key parameter for describing nonlinearity. Recent work has explored estimating wave height directly from monocular video [43, 4], and using stereo photogrammetry [13], but in most optical remote sensing configurations, individual wave heights remain unknown.

Chapter 2
METHODS

2.1 Observations

The data used in this analysis was collected during the DUNEX (During Near Shore EXperiment) field campaign from September to October 2021 at the US Army Corps of Engineers' Field Research Facility (FRF) in Duck, NC. A variety of in-situ and remote-sensing instruments were deployed during the experiment to investigate nearshore wave dynamics and changes to beach morphology during storm events.

This work focuses on imagery collected from the 43-meter FRF Imaging Tower located to the right of the pier in Figure 2.1 using an Argus system [39]. The system includes six PointGrey Flea2 cameras, which collect 17 minutes of imagery at 2 Hz every 30 minutes during daylight hours. Each camera captured 2048×2448 pixel images, which were converted from RGB to grayscale and rectified to a 1 m × 1 m grid using open-source tools by Bruder and Brodie [19] and McCann et al. [53]. Images captured simultaneously from all six cameras were then merged to produce composite image products covering 1600 m alongshore and 500 m cross-shore.

During the experiment, several problems with the Argus system arose, affecting image quality. Issues with the system's auto-exposure settings caused each camera to expose frames differently. When the images were merged and rectified, this created visible seams between the cameras. Challenges with the acquisition software also prevented some cameras from capturing frames at the desired 2 Hz frame rate. In the processed imagery, this manifests as flickering patches of missing data over part of the frame.

Regular bathymetry surveys were collected using the Lighter Amphibious Resupply Cargo (LARC) vehicle. The LARC surveys bathymetry with an accuracy of up to 2 cm using an

Figure 2.1: An aerial view of the field site for the DUNEX experiment at the Field Research Facility. Key landmarks include the pier and the imaging tower at the right edge of the property.

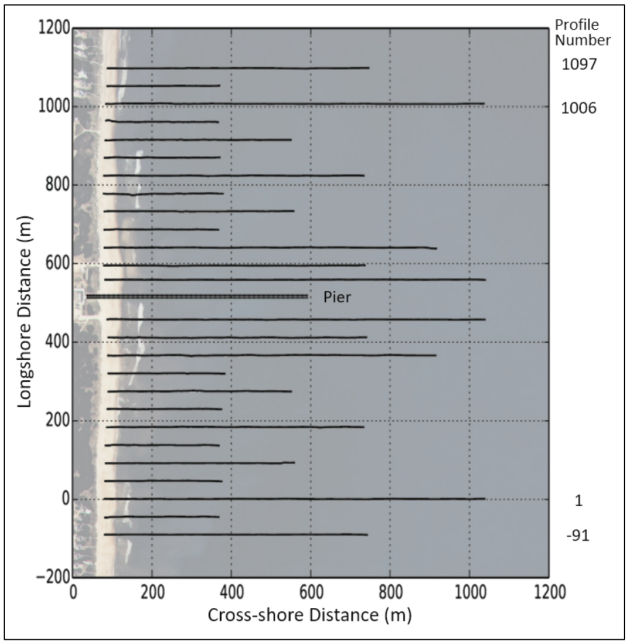

Figure 2.2: The FRF coordinate system reference. Reproduced from *Field Research Facility: A User's Guide to the Survey Lines Dataset* [15].

acoustic sonar and RTK-GPS [32]. These surveys were gridded and processed into digital elevation models (DEMs) at resolutions of 12 m cross-shore and 24 m alongshore. The surveys show a persistent but variable bar, with an average crest elevation of −1.5 m and a bar height of 0.9 m [68]. Water levels and bathymetry are referenced to NAVD88.

The FRF local coordinate system is oriented with the Y axis parallel to the shore at 18°, and the X axis normal to shore [15]. The most obvious features in the Argus imagery are the pier at $y_{\mathrm{FRF}} = 510\,\mathrm{m}$ and waves breaking over the bar at $x_{\mathrm{FRF}} = 150\,\mathrm{m}$, shown in Figure 2.2.

Contextual data of the incident wave conditions is taken from a long-term array of pressure transducers located at the 8-meter isobath, located approximately 900 meters offshore, and the nearshore CDIP buoy 433 in a water depth of 17 meters. Over the course of the experiment, wave heights varied from small to moderate (0.2 to 3 m), and approached the beach from a variety of directions ranging from shore-normal to grazing, as shown in Figure 2.3.

2.2 Detecting Breaking Waves

The diverse environmental and lighting conditions experienced over the month-long experiment include storms, varying sun angles, and a broad range of wave heights. This variety creates a challenging dataset for any traditional threshold-based image processing. A sample of timestacks from across the experiment is shown in Figure 2.4. Even within a single 17-minute Argus record, the kilometer-scale extent of the beach covered by the cameras results in vastly different lighting conditions and visual expressions of breaking and persistent foam. Manually identifying brightness or gradient thresholds to identify breaking waves for a single frame is challenging. Finding thresholds that hold over a month of varied lighting, cloud cover, and wave conditions is infeasible.

A machine learning approach is preferable, as a model can fit robust parameters across a wide variety of conditions. Instead of manually adjusting thresholds, the model is trained using supervised learning on labels from a subset of manually annotated breaking waves. Examples of these labels are shown in Figure 2.5. Another benefit of this approach is that updating the model to handle new conditions requires only annotating a small set of

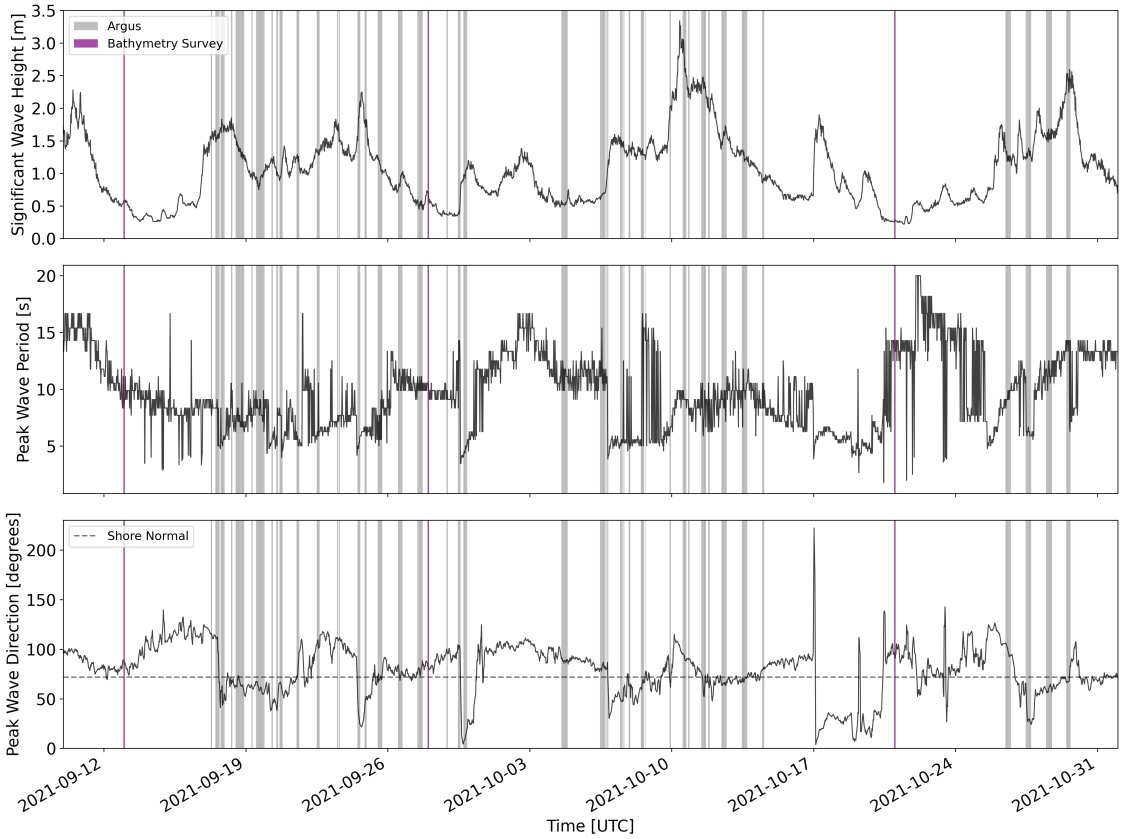

Figure 2.3: A time series of wave conditions during the DUNEX experiment from CDIP 433 showing a) significant wave height, b) mean wave period, c) mean wave direction [1]. Argus collection times are overlaid in gray, and bathymetry surveys in purple.

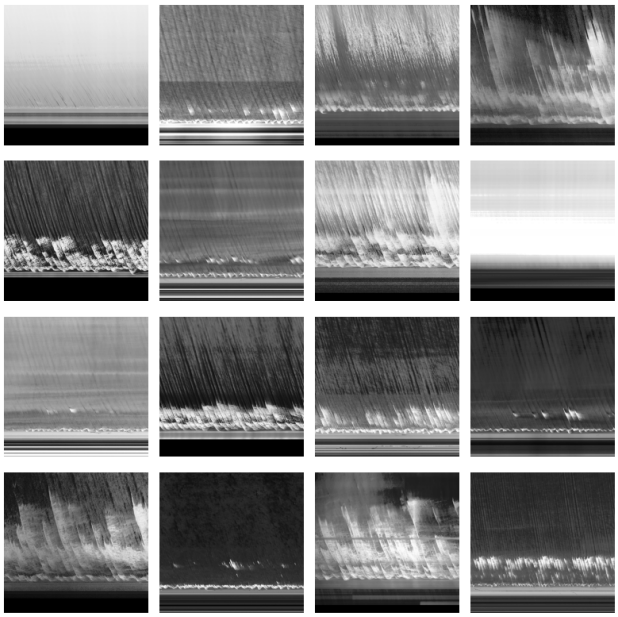

Figure 2.4: A sample of timestacks from across the experiment showing the range of lighting and wave conditions.

additional data to finetune the model on the new distribution.

Building on previous work that detects the breaking signature in timestack images using classical computer vision methods, and on more recent work that uses a combination of machine learning and heuristic thresholds to classify breaking, this work proposes an end-to-end machine learning technique that explicitly detects active wave breaking in timestack images. This removes tunable parameters, like the breakpoint detector in Lange et al. [44], pushing the classification decision into the model and onto the labeled training dataset. Timestack images have strong spatio-temporal gradients, making them easy to annotate and providing a clear signal for the algorithm to detect.

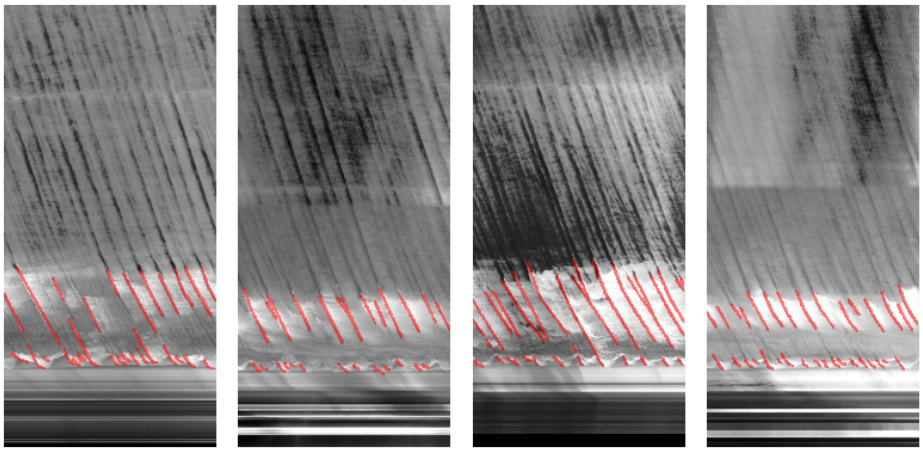

Figure 2.5: Four timestacks from the training dataset with labels overlaid in red. These samples show a variety of lighting conditions and exposure differences between cameras.

2.2.1 Dataset Curation

The dataset of 110 hours of video from September 17 to October 29, 2021, was first categorized by image quality. Low-contrast images, recordings with sensor dropout, or intense glare were excluded from the training dataset.

Five high-contrast Argus videos with clear breaking signatures from October 13th, 14th, and 28th were selected as the training set. Sections with sensor dropout were removed, and the remaining frames were uniformly sampled in space and time. The selected frames were manually annotated in the CVAT labeling tool [70] to create binary masks for pixels containing breaking waves. From this dataset, 332 timestacks (500 m $\times$ 128 s) were labeled.

While the training dataset is a small subset of the original, month-long collection, these five records still capture variety in wave conditions. The dataset is biased toward intermediate height waves from the northeast, with H_s from 0.8–1.5 m, T_p from 9–12 s, θ_p from 60–70°, and $\cos^2\theta$ from 18–20°. Visually, the training dataset is biased toward clear breaking signals but still covers substantial variability in lighting conditions due to the beach's spatial extent, which modifies the relative camera-to-sun angle. Varying this angle changes the Modulation

Transfer Function (MTF) drastically across the scene [89]. In some lighting conditions, the reflectance of the unbroken waves is so high that the glare saturates the camera sensor, making the diffuse reflection of the broken waves appear dark.

The labeled transects were sampled to generate training and validation datasets. Patches were sampled from the labeled images at the model input resolution 128×128-pixels and oversampled with 128 patches per 500×256-pixel image. Oversampling ensures the model learns spatial invariance, the surf zone is well sampled, and there are sufficient images for data augmentation.

A separate evaluation dataset of 30 videos was curated, spanning the month of the experiment. This dataset covers a broader range of conditions and spans substantial morphological changes to the beach. This data was not used in developing the algorithm and was used as a test case for applying the method to new data.

2.2.1.1 Data Augmentation

Image manipulations were applied to the training data to emulate the lighting conditions and data quality issues observed in the broader dataset. These more challenging images with adverse lighting and data dropout were explicitly excluded from the labeled training set to reduce labeling difficulty. Emulating these effects programmatically expanded the training dataset to capture a representative range of conditions while minimizing the amount and difficulty of labeling required. These manipulations included variations in brightness, contrast, and gamma to simulate changing lighting conditions, glare, streaks to emulate water droplets on the lens, and regular masking patterns to mimic camera dropout. Examples of each augmentation are shown in Figure 2.6. No flips or rotations were applied because the imagery has a fixed orientation.

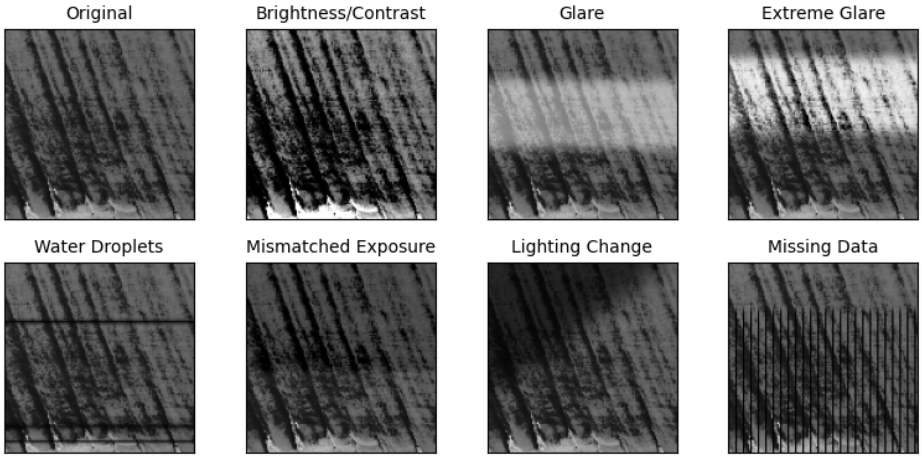

Figure 2.6: Examples of the data augmentations applied to a single image from the training dataset.

2.2.2 Machine Learning

2.2.2.1 Algorithm

The U-Net model by Ronneberger et al. [67] was one of the early successes in image segmentation. It remains a popular option for segmentation tasks due to its simplicity and ease of training. U-Nets are encoder-decoder networks. The encoder half of the network takes an input image and reduces its dimensionality through a series of convolutions and pooling operations to a vector of high-level features. The output side, or decoder, reverses these operations using a matching set of convolutions and up-scalings to generate pixel-wise predictions. A schematic representation of this architecture is shown in Figure 2.7a. The key insight of Ronneberger et al. [67] was that providing the input of each down-sampling operation to the corresponding up-sampling operation allows the model to learn weights that preserve high-resolution detail in the prediction while leveraging the broader context of learned features in the latent space, which contain information from across the image.

The implementation used here is based on Usuyama [85], which uses a ResNet [35] encoder. Residual Networks, or ResNets, use a technique similar to skip connections where

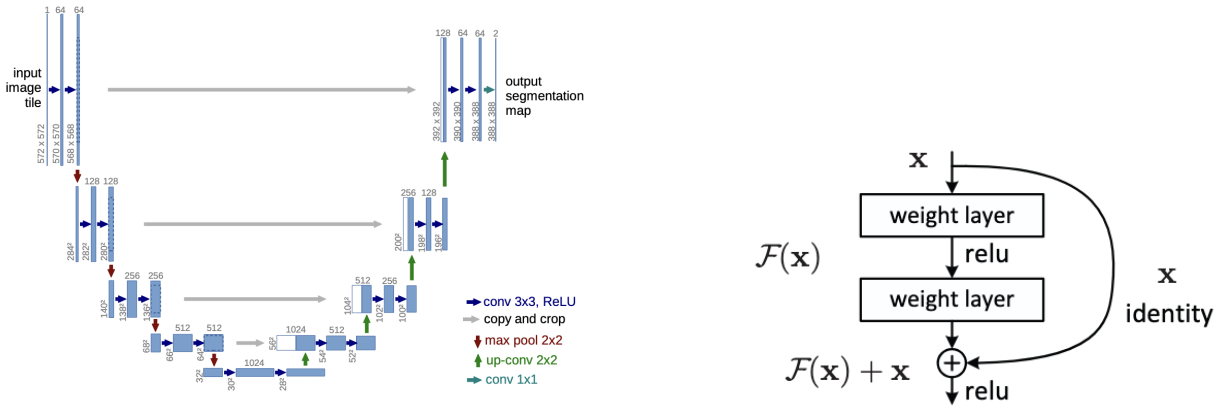

(a) U-Net architecture

(b) Residual block

Figure 2.7: Key architectural components: (a) U-Net architecture for segmentation tasks, reproduced from Ronneberger et al. [67], and (b) residual blocks for improved gradient flow in deep networks, reproduced from He et al. [35].

input to a block of convolutional layers is concatenated with its output before further processing. Shown in Figure 2.7b, He et al. [35] find that this improves training by improving the numerical stability of the gradients, allowing deeper networks.

Additionally, by selecting a well-developed architecture, such as a ResNet, as the backbone of the model, a pretrained encoder trained on the ImageNet1k dataset [28] can be used. These weights, trained on a large-scale classification task using millions of images, have encoded robust low-level image feature detectors. Initializing the model with these weights reduces the training and data requirements.

The network is trained with a combination of Dice and Focal losses to address the class imbalance in the dataset and to encourage accurate pixel masks. Focal loss was introduced by Lin et al. [46] to address the extreme class imbalance in foreground-background prediction tasks. It reshapes the binary cross-entropy loss function to reduce the influence of well-classified, easy samples in the background.

Focal loss takes a balanced cross-entropy loss for a prediction class probability p, where α is the inverse class frequency:

$$\mathcal{L}_{\mathrm{BCE}}(p) = -\alpha \log(p) \tag{2.1}$$

and adds a 'focusing parameter' $(1-p)^{\gamma}$ which, for positive γ values, decreases the loss as the model becomes more certain and the class probability approaches 1:

$$\mathcal{L}_{\mathrm{FOC}}(p) = -\alpha(1-p)^{\gamma} \log(p) \tag{2.2}$$

When balanced cross-entropy is adapted to Focal loss, the inverse class frequency α is less sensitive and is commonly set to 0.25. For this work, $\alpha = 0.25$, $\gamma = 2.0$ were used as recommended by Lin et al. [46] without further hyperparameter search.

Dice loss is based on the Sorensen-Dice index, or Dice similarity coefficient. This is analogous to the intersection over union (IoU) and is calculated as:

$$\mathcal{L}_{\mathrm{DSC}}(p) = 1 - \frac{2\mathrm{TP}}{2\mathrm{TP} + \mathrm{FP} + \mathrm{FN}} \tag{2.3}$$

It penalizes the model for both false positives (FP) and false negatives (FN), rewarding true positives (TP). Dice loss generally performs well under class imbalance with small objects, but is not as numerically stable as BCE or Focal loss [78].

The model was trained for 50 epochs using OneCycleLR [72] and the AdamW optimizer [48] with an initial learning rate of 0.005 and weight decay of 0.0001.

2.2.2.2 Class Imbalance and Bias

The dataset of breaking masks is significantly imbalanced due to the periodic nature of breaking waves and the small area of the surf zone in the image. Only 1.5% of the training dataset pixels contain breaking waves, which are distributed unevenly, biased toward the shore, and peak over the bar at 150 m.

U-Nets and other semantic segmentation models that operate on images smaller than the output resolution predict patches of a larger image, which are then stitched together.

To minimize artifacts, the patches are tiled with an overlap to minimize differences at the edges of the prediction. In this case, due to the uneven distribution of breaking waves in the image, any given patch is more likely to contain breaking on the shoreward side. To minimize artifacts from this bias in the tiled patches, the prediction for each patch is averaged with that of a randomly offset patch. Tiling and this averaging dramatically reduce the effect of the bias, but further work may remove it from the model during training. This could be achieved by enforcing invariance in predictions across the image tile.

2.3 Calculating Speeds

The model generates a binary mask for each timestack image, identifying pixels containing breaking waves. This mask of breaking pixels is then grouped into discrete clusters of contiguous breaking pixels, each capturing a single breaking crest.

The speed of each crest is estimated as the derivative of a cubic spline fitted to the mean cross-shore location of the mask in each frame. This spline-based approach smooths local variations in speed, but produces a continuous estimate of wave speed while preserving the broad structure of speed changes as waves cross bathymetric gradients.

The speed of a crest measured in the cross-shore transect does not capture the full wave celerity, which may additionally have an alongshore component, but given the high incidence angle of incident wave directions to shore normal, and tendency of refraction to increase this angle in the surf zone, this error is less than 5% of the speed.

Individual realizations of wave speed are averaged at each pixel over an Argus record to produce a robust map of breaker speed. Figure 2.9 shows that this average resolves variations in speed over and along the bar feature, approximately 150 m offshore, and in the swash.

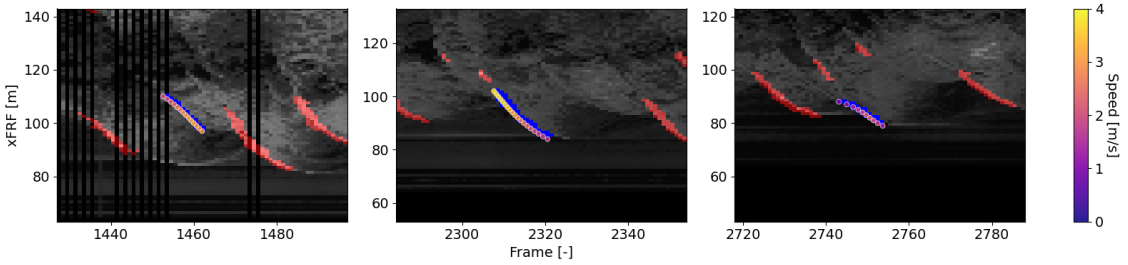

Figure 2.8: A visualization breaking pixel detections, spline, and calculated speeds overlaid on timestacks

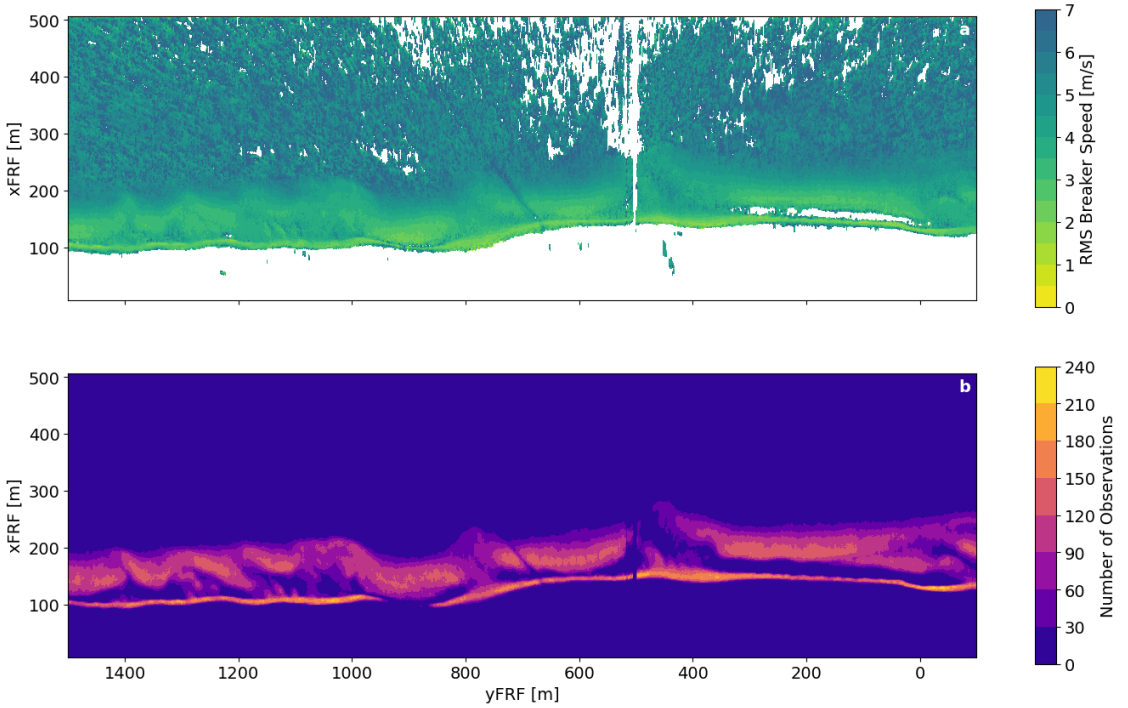

Figure 2.9: a) Average breaker speed and b) total number of observations over the 1 m grid for a 17-minute Argus record. Variations in speed over the bar are well resolved. Average speeds offshore of the bar are noisy, but represent a small fraction of the total observations.

Chapter 3

RESULTS

The breaker detection algorithm was applied to all 30 videos in the evaluation dataset, producing a breaking mask for every video frame. Speeds were then estimated for each of the 10.2 million detected breakers.

This dataset lacks ground-truth measurements for both breaking waves and bore speeds, so instead of directly evaluating the performance of our breaking wave detection model via pixel-level prediction accuracy, the results are evaluated against known surf-zone products, like timex and the survey bathymetry collected during the experiment.

3.1 Breaking Rates R_b

Integrating breaker detections from a record produces a result similar to a timex image, highlighting regions of regular breaking. The pixel-wise breaking rate, R_b, can be calculated by normalizing the number of detections by the record length. Like a timex, this breaking-rate measurement reveals the spatial distribution of breaking, showing the locations and widths of sandbars. Additionally, it quantifies the intensity of breaking and removes the influence of remanent foam, linking the measurement more closely to dissipation. Figure 3.1 shows how R_b describes the same area of breaking as the timex, and additionally shows regions of intensified breaking along the bar and subtle alongshore variations in the bar and beach face.

The breaking rate approximates an important surf-zone parameter, Q_b, the fraction of broken waves. Thornton and Guza [82] use Q_b to parametrize dissipation throughout the saturated surf zone. This method does not count unbroken waves, so the classical Le Mehaute [45] ratio, $Q_b = N_{\mathrm{br}}/N_t$, cannot be applied, but the fraction of broken waves can be estimated

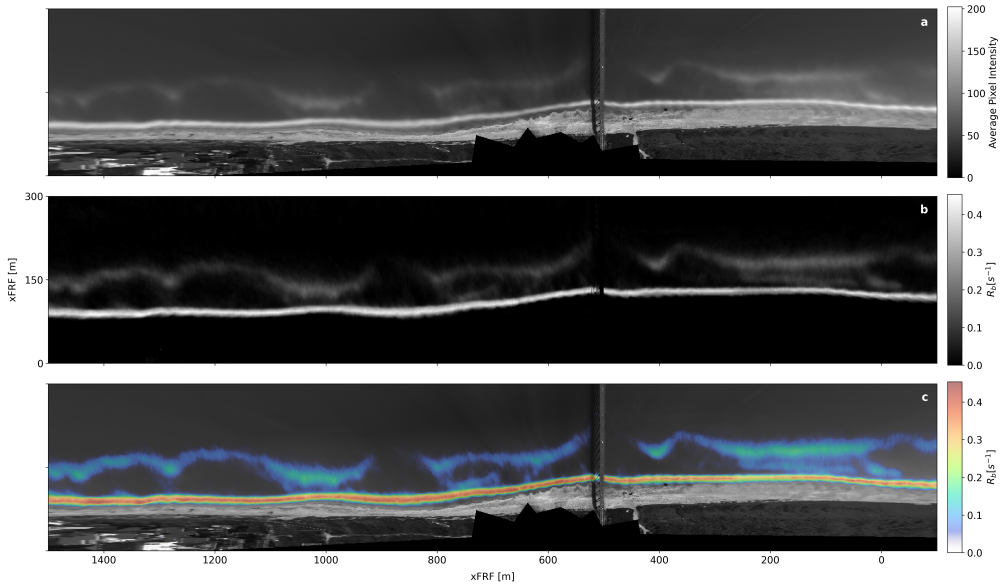

Figure 3.1: A comparison of a) 17-minute timex, b) breaking rate (R_b) from this method, and c) an overlay that highlights the agreement between the two methods, and the additional detail visible in R_b.

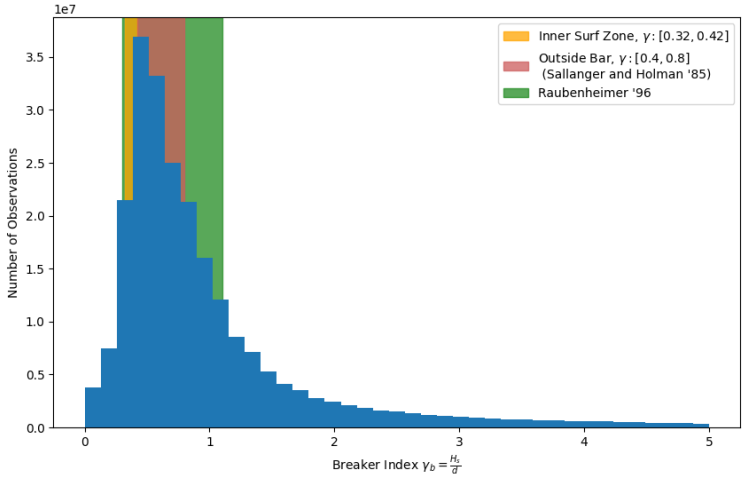

Figure 3.2: A histogram of breaker indices calculated from offshore significant wave height. Sallenger Jr. and Holman [69] found values ranging from 0.32 to 0.80 at the Field Research Facility

using the peak period as $Q_b = N_{\text{br}}/N_{T_p}$ [74]. Further discussion of the application of this Q_b product to dissipation estimation is continued in Appendix A.

3.2 Breaker Index

To quantitatively evaluate the area of breaking, the breaker index is compared against expected values for the FRF. Breaker index is calculated using the offshore significant wave height because individual wave heights throughout the surf zone are not available. Despite this approximation, Figure 3.2 shows that the estimates of γ compare favorably to the canonical ranges, with the peak falling in the expected range of 0.3–1.1 [65]. A right-skewed, long-tailed distribution is expected when using offshore wave height, as in the shallow water of the inner surf zone, $H_{s_{offshore}}$ will be unrealistically high and no longer representative due to wave breaking.

3.3 Breaker Speeds

The accuracy of the detections is evaluated by comparing the estimated speeds with theoretical models using water depth from surveyed bathymetry. Figure 3.3 shows the density distribution of observed speeds across the dataset against the surveyed depths. The bulk of the observations lie near and slightly above the speed predicted by linear theory, with wide scatter and three notable distinctions.

First, in shallow water, speeds do not converge to zero. In shallow water, nonlinear effects that increase speed relative to linear become increasingly important as the bore height approaches the water depth. Swash and uprush dynamics may also explain some of these high velocities, while bad detections and speed estimates account for others. Breaking waves above the zero water level are attributed to bad detections, errors in bathymetry, and run-up.

Second, in the surf zone, there are specific depths with broad ranges of speeds, visible as vertical bands in the histogram. These depths correspond to the onset of breaking under the various wave conditions and are an artifact of the speed calculation, which is sensitive to the shape of the mask at the onset of breaking.

Third, offshore, there are two populations: one that roughly follows the linear curve and a second broad distribution of waves significantly below the linear wave speed. These are a combination of bad detections with non-physical speeds and whitecapping, in which speed is not a function of depth but rather of breaker scale and is typically less than the phase speed [33].

Throughout the surf zone, the mean breaker speeds exceed the linear wave speed. As discussed by Inman et al. [41], this is expected due to the effects of nonlinearity and the contribution of breaker height to the effective water depth.

Normalizing depth by the offshore wave height, as in the γ calculation in Section 3.2, data from across the varying wave conditions can be consolidated and compared against bore speed models. In Figure 3.4, entering the surf zone ($\gamma > 0.3$), the average speed begins to exceed the linear wave speed. Progressing from the surf zone to the inner surf zone ($\gamma > 1.1$)

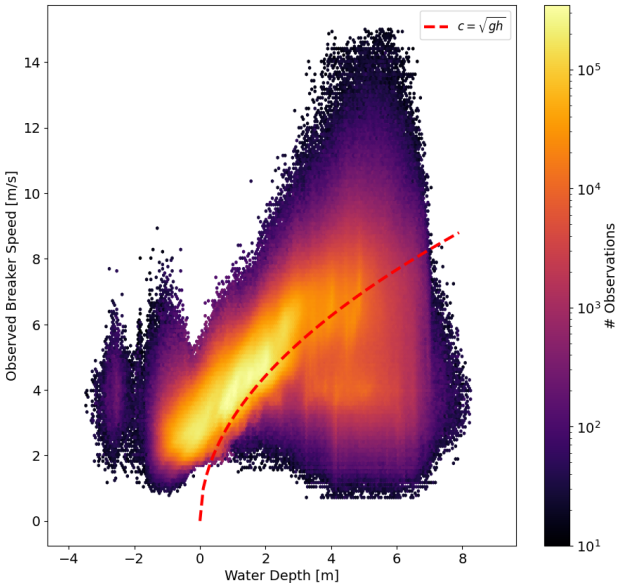

Figure 3.3: A histogram of breaker speed and water depth with linear wave speed, $c = \sqrt{gh}$, plotted in red. Negative depths are breakers above the tide-adjusted water level, and vertical bands correspond to the spread observed at the onset of breaking.

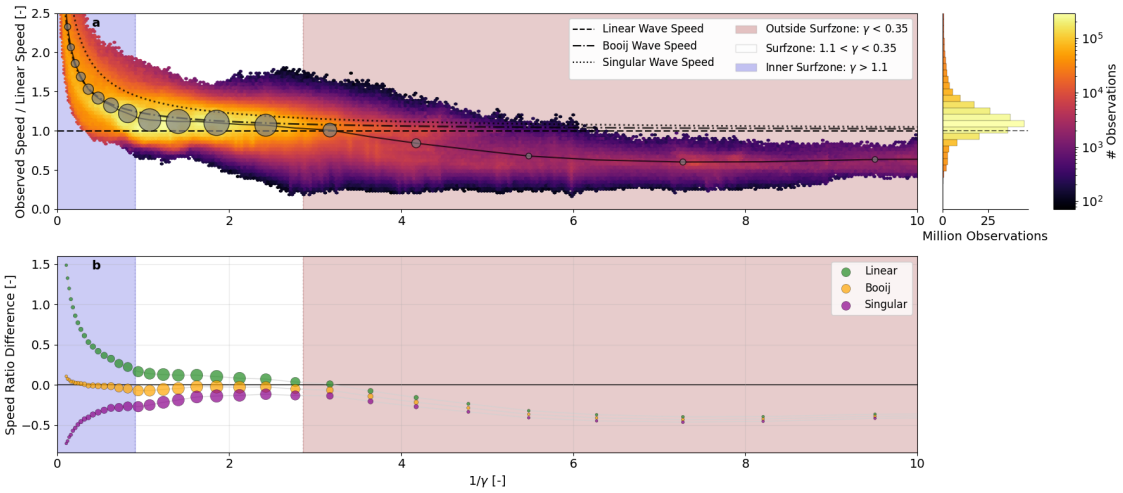

Figure 3.4: A comparison of bore speed models. a) A histogram of all speed observations plotted against their normalized depth, $1/\gamma$. The mean is shown as gray circles. b) Residuals from the speeds predicted by the various bore models. The Booij model has the best agreement with the observed speeds.

speed is increasingly well described by the Booij bore model $c_p = \sqrt{gh + H/2}$, or in terms of γ, $c_p = \sqrt{gh \cdot (1 + \gamma/2)}$.

The speed distributions for these regions are shown in Figure 3.5. In the inner surf zone, observed speeds greatly exceed the linear speed, and as nonlinearity increases, the bias decreases. In the surf zone, the speeds slightly exceed the linear speed, and the Booij correction minimizes bias. Outside the surf zone, the distribution is bimodal, with one peak near the linear speed and one broad peak substantially slower that may correspond to whitecapping or false detections.

3.4 Speed Calculation Sensitivity and Bias

The speeds of the detected breakers are well described by Booij's nonlinear modifications to shallow water wave speed, but the variance in observed speeds is high. The leading cause of this spread is error introduced by the shape of the ML-generated masks shown in Figure 3.6.

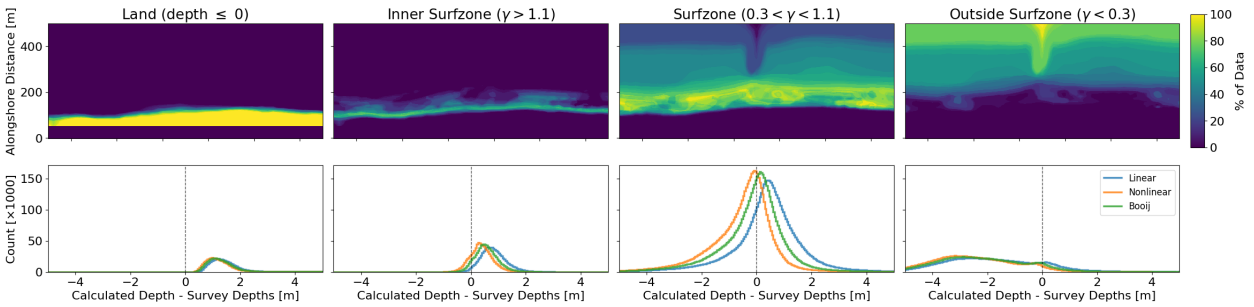

Figure 3.5: The distribution of surf-zone regions defined by $\gamma = H_{s_{\text{offshore}}}/h$ and residuals of bore speed models.

To reduce the discretization effects of the 1 m $\times$ 2 Hz gridded images on the slope of the timestacks, cubic splines were fit to estimate the slopes of the data and speed of the bores. The continuous derivative of the splines provides a more robust estimate of the slope, but the spline fit remains sensitive to slight differences in the shape of the classification mask at the start and end of the feature.

The results for three methods for calculating the slope are shown in Figure 3.7. Each introduces different types of bias along the average breaker track. For all methods, the speeds are close to those predicted by linear theory. However, especially at the start and end of each detection, the bias is high. Even small changes to the slope calculation change the nature of this bias along the detection. These biases along the breaker track length are aliased into spatial patterns because of the distribution of breaking shown in Figure 3.8. Wave breaking initiates on rising slopes and stops over troughs, terraces, and the swash. Averaging the temporal bias over this spatial distribution of breaking produces the spatial bias in speed shown in Figure 3.2.

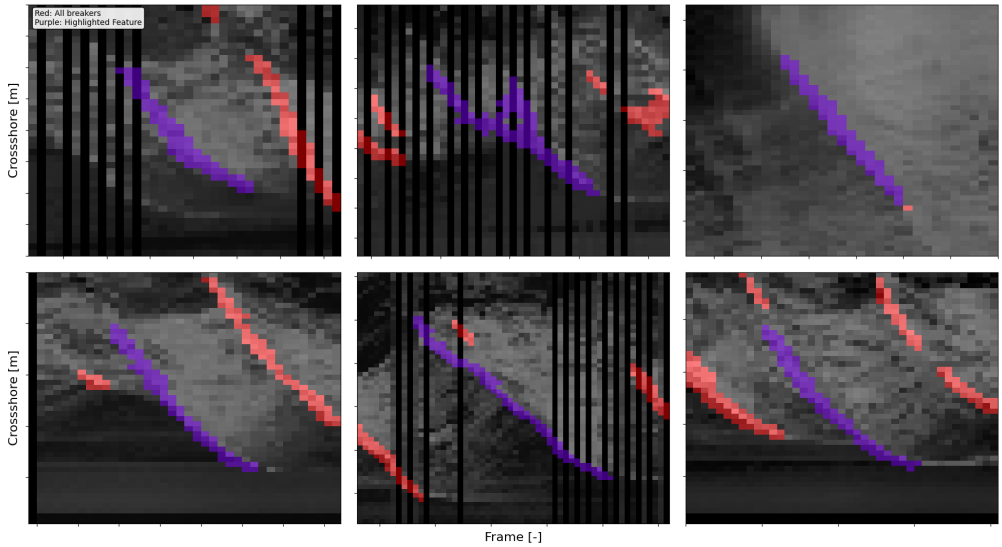

Figure 3.6: A sample of identified breakers. This close-up view highlights how small errors at the end of a detection can have a large impact on the calculated slope.

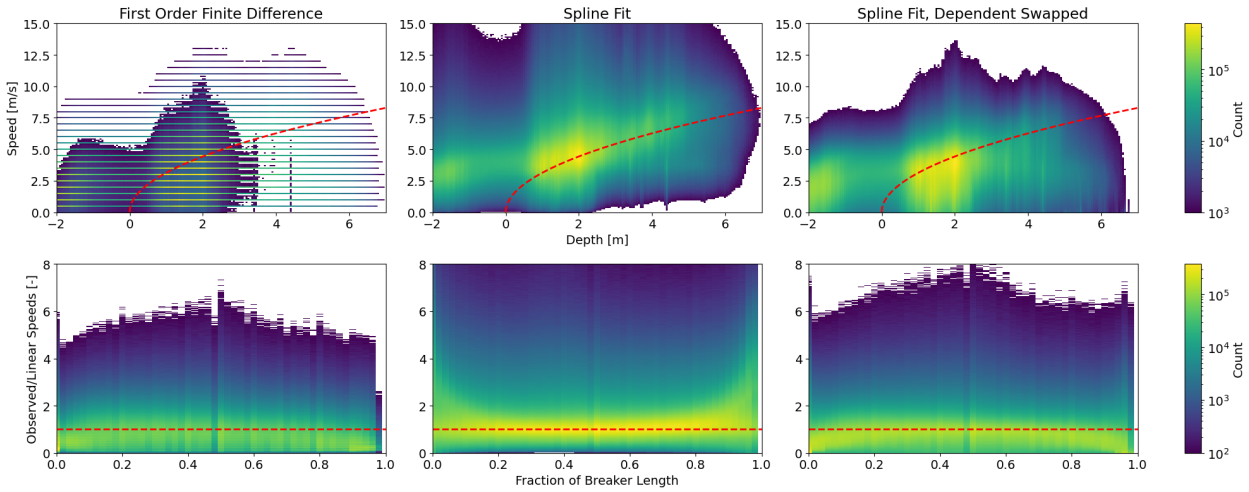

Figure 3.7: Results from three different speed calculations are shown. The first row shows a histogram of speed and depth, which highlights the biases of each method. The second row shows speeds normalized over the length of a breaking crest, showing bias relative to the location within the detected breaking wave.

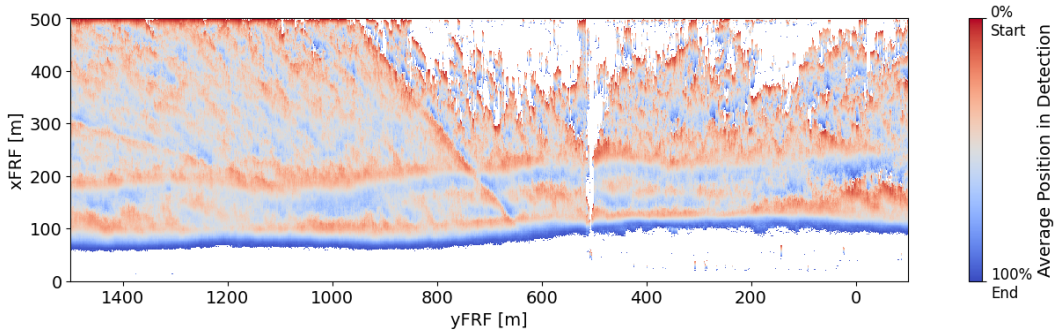

Figure 3.8: The spatial distribution of the average point in the duration of a breaking event for all detections in one Argus record. The colored regions highlight areas where breaking begins on the bar and foreshore, and ends in the trough and swash.

Chapter 4

DISCUSSION

4.1 Inverted Bathymetry

One application of these measurements of breaking-wave speed is bathymetry estimation. This follows a long history of celerity-based bathymetry inversion discussed in Section 1.5.5, and builds on recent work by Lange et al. [44], which uses breaking celerity to estimate depth in the surf zone where cBathy struggles [38]. The 1 m resolution of this method's speed estimates can resolve alongshore variability in the surf-zone bathymetry and capture complex morphology, including bars and terraces.

In Section 3.3, we find that the Booij bore model describes the bulk of the breaker speeds estimated by this method. Using the Booij model, we formulate the inverse problem of estimating bathymetry by solving the celerity equation for depth.

$$h = \frac{c^2}{g(1+\gamma/2)} \tag{4.1}$$

A gamma value of 0.35 is used based on existing literature [65] and supported by the earlier analysis shown in Section 3.2. Using this equation, depth is estimated from each realization of breaker speed and averaged across the record.

A qualitative inspection of the inverted depths in Figure 4.1 shows depth decreasing towards the shore. A bar feature with alongshore variation in location, width, and depth is present between $x_{\mathrm{FRF}} = [150, 200]$ m. Estimates offshore of the bar are noisy and biased shallow. Moving alongshore, the beach changes from terraced to barred with variations in beach slope. Inspecting individual transects, we find bar and terrace features are biased shoreward by 10–20 m. The depths of the beach face and offshore bar slope are overestimated. These errors match the expected bias from the patterns in speed observed in Section 3.4.

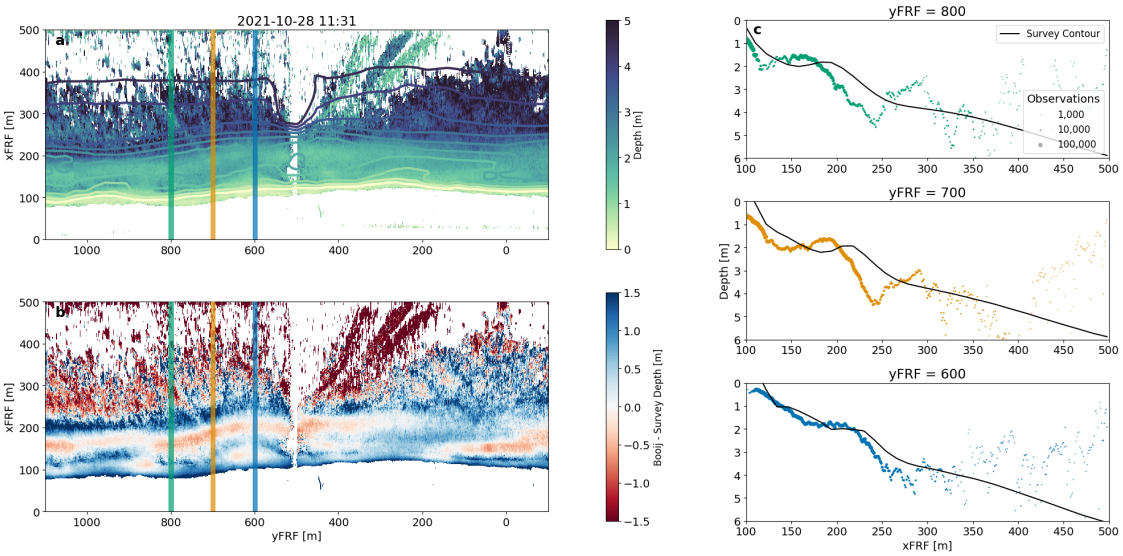

Figure 4.1: Inverted depths using Booij bore celerity. a) Estimated depths overlaid with survey bathymetry contours show cross-shore and alongshore variability. b) Error in estimated depth. c) 10 m alongshore-averaged transects highlight differences in bar morphology that are resolved despite the systematic errors.

The survey contours for the transects in Figure 4.2 vary over the course of the experiment in response to changes in wave forcing. The estimated depths follow these bathymetric trends. Starting with the 800 m transect, the crest of a steep bar is located at 150 m, at a depth of just under 1 m. The inverted depths show the crest slightly shoreward at 125 m, but at the correct depth. In the subsequent survey, the bar crest has moved offshore to 180 m and deepened to 1.5 m with a less pronounced trough. Although still biased shoreward, the inverted depths capture this offshore movement and deepening of the crest. In the third survey, the bar has flattened and no longer has a trough; it has also moved further offshore. The estimated depths capture the offshore movement of the crest, but overestimate the presence of a trough at 125 m.

At the 700 m transect, the profile starts moderately barred, with a terrace at 140 m. The estimated transects are accurate over most of this profile, but are biased too shallow over the terrace beginning at 125 m, and too deep at the offshore edge of the bar at 200 m. In the following survey, the estimated depths accurately resolve the bar, newly developed trough, and beach face. Depth is overestimated at the offshore edge of the bar. In the final survey, the bar is farther offshore and has developed a more pronounced, wider trough. The inverted depths resolve the offshore movement of the bar and continue to overestimate depth at the offshore extent of the bar, but underestimate depth over the crest of the bar.

The 600 m transect exhibits a similar temporal evolution to that of the 700 m transect. The notable difference is that the inverted depths are bimodal. One group captures the September 17 survey profile with biases similar to those observed in the other transects, while the other realization shows the bar deeper and substantially farther offshore. The subsequent survey on September 29 shows the bar deepening and moving offshore, but given the method's uncertainty, it is difficult to attribute this change in profile to actual morphological change.

4.1.1 Patterns of Error in Inverted Bathymetry

Distinct patterns in error are visible in the transects shown in Figures 4.2 and 4.3. The method overestimates the depth on rising slopes where breaking typically begins. Over the

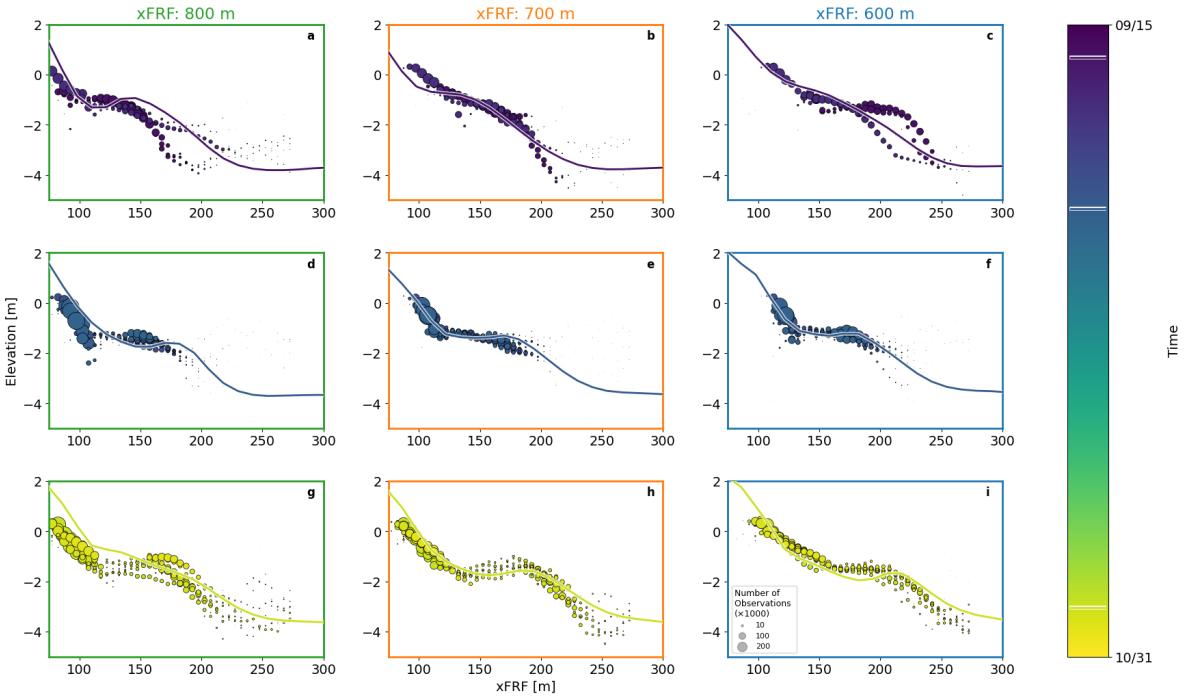

Figure 4.2: Temporal evolution of the transects from Figure 4.1, grouped by survey date. Despite the shoreward bias of bar location and variability, the results resolve changes to bar shape and location.

sandbar, depth estimates have < 1 m error, but the tendency to overestimate depth on the outer edge and to underestimate depth in the trough shifts the bar shoreward. Offshore depth is substantially overestimated, especially beyond the 3 m isobath.

Using the same γ groupings from Figure 3.5, bathymetric error is quantified across these regions in Figure 4.4. Most observations lie in the surf zone, where depth is predicted with low bias but high variance. Moving shoreward, the model increasingly overpredicts depth. Offshore, a small subset matching the linear speed is well predicted, while the larger distribution is biased shallow. Poor offshore performance is expected, as our inversion method is based on depth-limited breaking, which is infrequent outside the surf zone. In practice, areas without depth-limited breaking can be easily filtered based on a minimum R_b or a

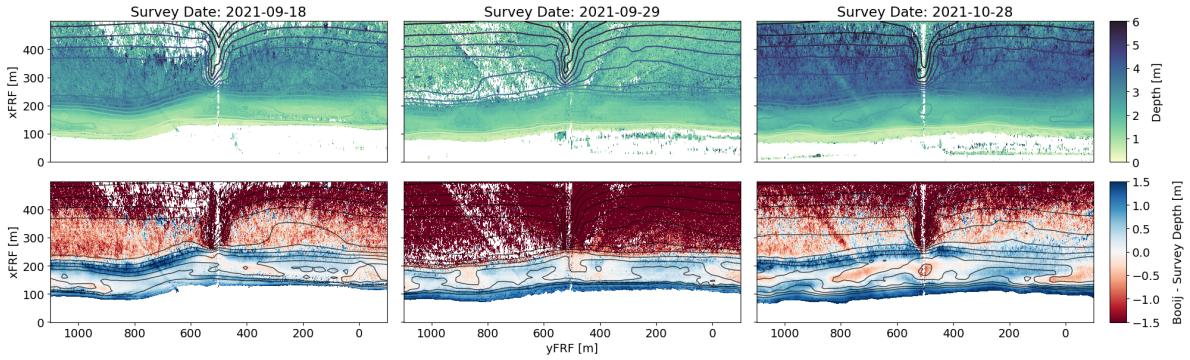

Figure 4.3: The first row shows maps of inverted depths overlaid with contour lines from the most recent survey. The second row shows errors in the generated bathymetry. For each survey, depth is overestimated at the offshore edge of the bar and the beach face, and underestimated at peaks in the bathymetry over the bar.

maximum γ, thereby complementing existing bathymetry inversion techniques that perform well outside the surf zone (e.g., cBathy).

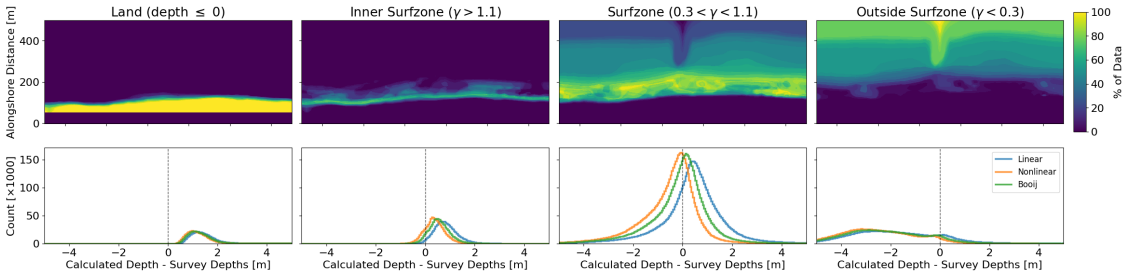

Figure 4.4: The distribution of surf-zone regions defined by γ and depth error over these areas.

4.2 Performance

To improve model performance, particularly in iterative machine learning frameworks, understanding correlations between errors and environmental factors can guide the labeling of

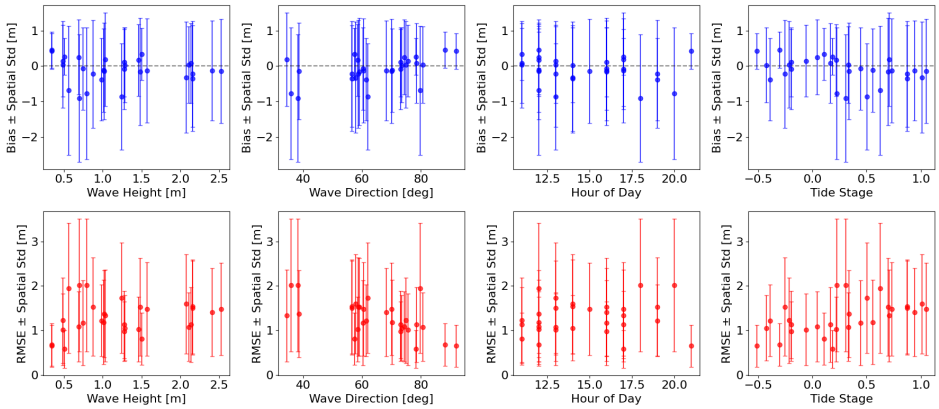

Figure 4.5: The first row shows bias as a function of significant wave height, mean wave direction, time of day, and tidal stage. The second row shows RMSE as a function of the same parameters, showing no significant trends, except for a modest increase in RMSE with tide stage.

additional training data. Trends correlated with environmental factors would suggest overfitting to biases in the training dataset, under-representation of real-world conditions, or other limitations in the data and processing. No significant trends are observed in Figure 4.5 with respect to wave conditions, lighting, or date of bathymetry survey. The mean bias is less than 1 m across all cases, but as discussed in Section 4.1, the systematic nature of the bias shifts features like the bar shoreward. RMSE is high, generally >1 m, consistent with the systematic bias and weakly correlated with the tide stage.

4.3 Practical Considerations

4.3.1 Designing the Machine Learning Task

As shown in Section 3.4, the estimated slope is sensitive to errors of a few pixels in the detection mask. Several factors exacerbate this problem. The dataset's resolution (1 m × 2 Hz) means these errors correspond to significant changes in estimated speed. Pixel-accurate masks are challenging to achieve in machine learning algorithms, as the loss function must

balance accuracy and numerical stability. The use of Dice and focal losses, which penalize IoU and per-pixel predictions, respectively, aims to strike a balance that is sensitive to minor errors in the detection mask while yielding a smooth loss surface for optimization. Additional loss terms, such as the boundary loss term from Ronneberger et al. [67], may improve the accuracy of detected masks. Human labelers also struggle to generate pixel-perfect labels. Under favorable lighting conditions, it is trivial for a labeler to identify breaking waves, but especially at this resolution, tracing pixel-perfect masks is time-consuming and often ambiguous.

Potential future improvements to address these limitations include increasing both spatial and temporal resolutions, training a model to predict the bore toe or wave speed explicitly. These options all come at an increased cost, paid in labeling time, training stability, and storage or computational efficiency.

A second challenge is segmenting individual bores in these noisy detections. The model used here predicts a binary mask for wave breaking that does not distinguish individual breaking waves. This mask is then segmented into individual wave crests using morphological operations that increase separation between features. This segmentation is challenging when waves meet and overtake, or are close enough in space and time that small errors in the mask connect adjacent waves. Such bore-bore capture events are infrequent, but are not resolved in this framework. Increased resolution would improve the separation of truly distinct waves, but more sophisticated processing would be needed to resolve these events, either by post-processing the detections, following Stringari and Power [75], or by switching to an instance segmentation model, in which individual waves are detected and masked.

4.3.2 Lighting Impacts

The performance of this method is sensitive to lighting conditions, such as sun angle and cloud cover. A key advantage of a machine learning approach is the ability to fit complex distributions by simply labeling more data or by modifying existing data to capture new conditions via data augmentation. With data augmentation, this training dataset is relatively

diverse, but the model still struggles under extreme lighting conditions, such as sun glare and very low contrast.

There are two distinct problems with these challenging lighting conditions. The first is a data problem: when the camera's dynamic range and gain correction are insufficient to expose the entire image, the sensor saturates, losing information in these regions. Other parts of these saturated images will have such low contrast that breaking waves are indistinguishable from the background. The second is a labeling problem. Even when the sensor has sufficient range to expose the image, labeling these images with high dynamic range is made more challenging by the camera's limited bit depth, which further compresses weak signals. Even with exposure, gamma, and contrast controls, identifying the breaking-wave signal remains subjective and ambiguous.

Adding a prediction class for poor image quality to the model could improve its performance on challenging data by training it to ignore these weak, uncertain signals. In practice, flagging this low-quality data would also allow high-quality measurements to be averaged over longer periods without contamination from noisy or incorrect predictions [26, 14]. This averaging would improve performance across a variety of conditions.

4.3.3 Generalization

The model was trained on a relatively small set of 332 labeled timestack images. The total evaluation dataset consists of 90,316 individual frames, each 1600 $\times$ 500 pixels, equivalent to over 550,000 training timestacks. Although each labeled image contains many instances of breaking, the training dataset is much smaller than the evaluation dataset (0.06%) and covers only a subset of wave and lighting conditions. Despite these limitations, the model accurately predicts breaking throughout most of the month-long dataset.

One compelling advantage of this machine learning approach is that the algorithm was easily adapted to handle missing data. Data acquisition challenges during the experiment resulted in a significant amount of the Argus data with missing data in part of the image. In timestacks, the visual discontinuity caused by the missing data makes labeling challenging.

Instead of discarding this portion of the dataset, the model was trained to handle dropout by simulating it on high-quality data using masking at representative rates. Enabling the processing of these images substantially increased the usable data available for final evaluation and yielded results over a larger set of the bathymetry surveys.

While the model has generalized from the limited training set to the range of conditions experienced during the month, which encompass waves from < 1 m to 3 m, larger shifts in the distribution or data such as changes to resolution in space or time, substantially different wave conditions, or running the model on data from a different beach will require finetuning or retraining on additional labeled data from the new conditions.

Chapter 5
CONCLUSION

This study develops an adaptable end-to-end machine learning method for detecting breaking waves in timestack images. The algorithm is robust to challenging conditions, including glare, rain, variable data rates, and diverse lighting. Data augmentation proves to be a valuable tool for improving performance across such varied data. Further improvements to breaker detection could be achieved with a larger, more diverse training set and more advanced machine learning techniques.

The breaking rate calculated from these detections complements traditional timex methods by separating active breaking from remanent foam, more robustly measuring the breaking area. Additionally, this rate can be used to calculate the breaker quotient, which could be used to estimate dissipation from the fraction of breaking waves.

Speeds calculated from the detected breaking crests are shown to fit within the expected range for bore propagation. They are well described by the Booij model, which includes a nonlinearity term based on the wave height. While in-situ wave heights are not available, the breaker index γ is found to be a reasonable proxy for the nonlinearity throughout the surf zone.

Using breaker speeds calculated from this method's detections, the Booij model is used to estimate water depth and map the surf-zone bathymetry. This depth estimate exhibits low but systematic bias and high variance in the surf zone. This bias results from sensitivity in the speed calculation to the shape of the breaking mask. Despite these limitations, the bathymetry profiles generated by this method compare favorably with surveyed bathymetry and qualitatively capture changes in beach shape over the month-long experiment.

The sensitivity observed in the breaker speed calculations highlights the need for careful

consideration of data quality and methods when measuring speeds from machine learning detections. The impact of this sensitivity could be mitigated by higher-resolution data, more accurate breaking masks for training, improved machine-learning techniques, or better post-processing to refine and filter detections.

These encouraging initial results demonstrate the potential of an end-to-end machine learning method for breaker detection to enable low-cost, regular measurements of breaking waves in the nearshore with broad applications to the study of wave-driven coastal processes in the field. Future applications include investigating the links between patterns and mechanics of breaking, and circulation [6, 5] and dissipation [52].

Appendix A

Q_B DISSIPATION ESTIMATES

Following Stringari and Power [74], the R_b from Figure 3.1 is interpreted as a breaking rate using the peak period T_p. Using this estimate for Q_b, we estimate dissipation following as [82, 83, 11]:

$$D = \frac{\alpha}{4} Q_b f_p \rho g H_{\max}^2 \tag{A.1}$$

The results from this estimate, shown in Figure A.1, are within the expected scale factor $\alpha = O(1)$ [11] of the incident wave energy flux. The breaking results are well correlated with the timex, suggesting that this method reasonably captures the distribution and along- and cross-shore variations in dissipation. A key limitation of this result is that it relies on the survey bathymetry to estimate wave heights $H_b = \gamma h$ through the surf zone, although in the future this could be derived from imagery as in this work, directly from imagery as in Almar et al. [4], Klotz et al. [43], or using a simple model of Q_b [82].

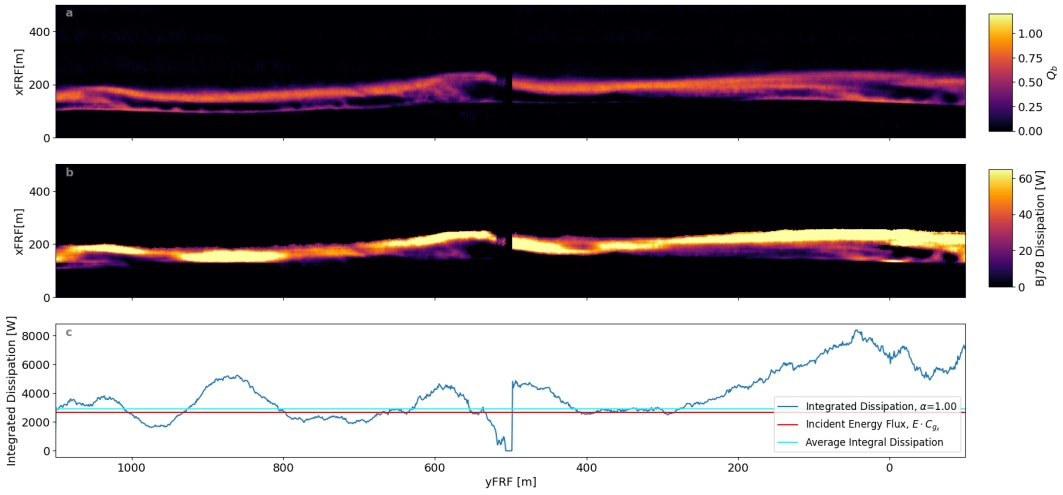

Figure A.1: Estimates of dissipation from Q_b. a) Q_b calculated as R_b/T_p. b) Dissipation estimated following Battjes and Janssen [11]. c) Cross-shore integrated dissipation falls within the expected O(1) scaling of the incident wave energy flux.

Appendix B

PARAMETRIC MODEL

To understand the Q_b results, studies were conducted using a simple analytical model that combined the Thornton and Guza [83] model for breaking and Q_b and the Battjes and Janssen [11] model for dissipation based on the wave height distribution $p(H)$. Detailed results for a single transect are shown in Figure B.1. This simple model was then applied to the wave rays generated by the Halsne et al. [34] ray-tracing model to create an analytical, but realistic map of Q_b across the beach Figure B.2. Wave energy flux was also calculated from this model to compare with the dissipation results from Appendix A. As with the incident energy flux, estimates from the observed Q_b and this analytical model are of the same magnitude across the beach in Figure B.3.

The ray-tracing model was also used to investigate alongshore variations in dissipation captured in the remote-sensing data. Again, the model produces qualitatively similar results.

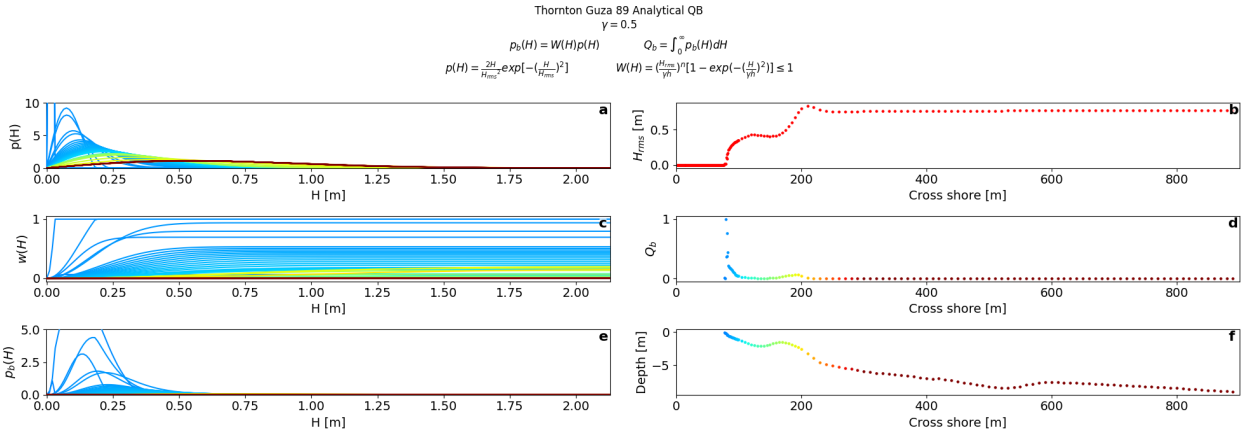

Figure B.1: An analytical model for Q_b following Thornton and Guza [83]. The wave height distribution $p(H)$ (a), is modified by $p_b(H)$ (b), the probability of breaking, calculated using the weighting function $W(H)$ (c), a soft thresholding on the original distribution based on depth h. Integral properties are shown as RMS wave height (d), which is modified by breaking Q_b (e) over the bathymetry (f).

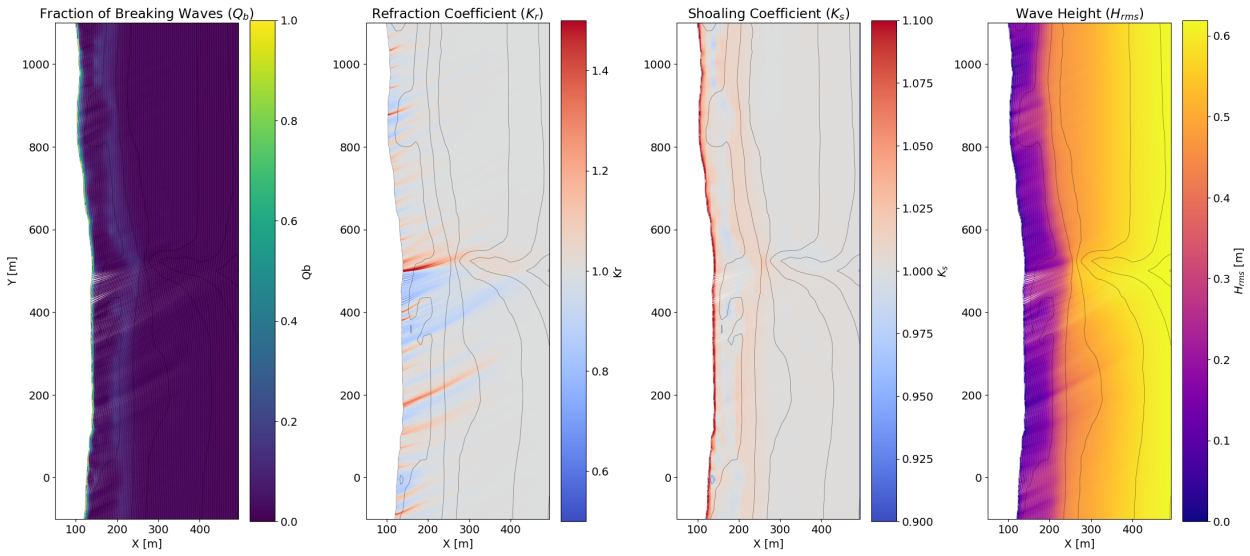

Figure B.2: Results of the analytical breaking model applied to wave rays. From left to right Q_b, the fraction of broken waves, K_r, the refraction coefficient, K_s, the shoaling coefficient, and H_{RMS}, wave height across the domain. These results, especially Q_b, are qualitatively similar to the R_b in Figure 3.1 with the highest values on the beach face, and a lower, broader peak across the bar.

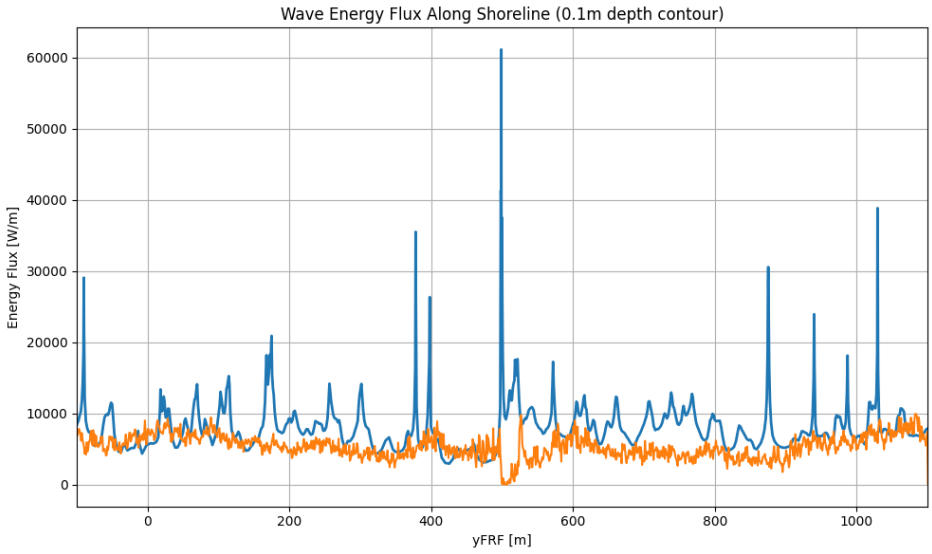

Figure B.3: Integrated wave energy flux from the dissipation results in Appendix A compared with the analytical model. There is a scale error in the observed flux (orange), and sensitivity to bathymetry resolution, but qualitatively, the results are of similar magnitude and share similar patterns in the alongshore distribution of energy.

BIBLIOGRAPHY

[1] CHL Field Research Facility Data Server, 2025. URL https://chldata.erdc.dren.mil/thredds/catalog/frf/catalog.html.

[2] S. Aarninkhof and B. Ruessink. Video observations and model predictions of depth-induced wave dissipation. *IEEE Transactions on Geoscience and Remote Sensing*, 42 (11):2612–2622, Nov. 2004. ISSN 1558-0644. doi: 10.1109/TGRS.2004.835349. URL https://ieeexplore.ieee.org/document/1356074. Conference Name: IEEE Transactions on Geoscience and Remote Sensing.

[3] S. G. J. Aarninkhof, B. G. Ruessink, and J. A. Roelvink. Nearshore subtidal bathymetry from time-exposure video images. *Journal of Geophysical Research: Oceans*, 110(C6), 2005. ISSN 2156-2202. doi: 10.1029/2004JC002791. URL https://onlinelibrary.wiley.com/doi/abs/10.1029/2004JC002791. _eprint: https://onlinelibrary.wiley.com/doi/pdf/10.1029/2004JC002791.

[4] R. Almar, E. W. J. Bergsma, P. A. Catalan, R. Cienfuegos, L. Suarez, F. Lucero, A. N. Lerma, F. Desmazes, E. Perugini, M. L. Palmsten, and C. Chickadel. Sea State from Single Optical Images: A Methodology to Derive Wind-Generated Ocean Waves from Cameras, Drones and Satellites. *Remote Sensing*, 13(4):679, Jan. 2021. ISSN 2072-4292. doi: 10.3390/rs13040679. URL https://www.mdpi.com/2072-4292/13/4/679. Publisher: Multidisciplinary Digital Publishing Institute.

[5] C. M. Baker, M. Moulton, C. C. Chickadel, E. S. Nuss, M. L. Palmsten, and K. L. Brodie. Two-dimensional inverse energy cascade in a laboratory surf zone for varying wave directional spread. *Physics of Fluids*, 35(12):125140, Dec. 2023. ISSN 1070-6631. doi: 10.1063/5.0169895. URL https://doi.org/10.1063/5.0169895.

[6] C. M. Baker, M. Moulton, M. L. Palmsten, K. Brodie, E. Nuss, and C. C. Chickadel. Remotely sensed short-crested breaking waves in a laboratory directional wave basin. *Coastal Engineering*, 183:104327, Aug. 2023. ISSN 03783839. doi: 10.1016/j.coastaleng.2023.104327. URL https://linkinghub.elsevier.com/retrieve/pii/S0378383923000510.

[7] T. Baldock, P. Holmes, S. Bunker, and P. Van Weert. Cross-shore hydrodynamics within an unsaturated surf zone. *Coastal Engineering*, 34(3-4):173–196, Sept. 1998. ISSN 03783839. doi: 10.1016/S0378-3839(98)00017-9. URL https://linkinghub.elsevier.com/retrieve/pii/S0378383998000179.

[8] M. L. Banner and O. M. Phillips. On the incipient breaking of small scale waves. *Journal of Fluid Mechanics*, 65(4):647–656, Oct. 1974. ISSN 1469-7645, 0022-1120. doi: 10.1017/S0022112074001583. URL https://www.cambridge.org/core/journals/journal-of-fluid-mechanics/article/on-the-incipient-breaking-of-small-scale-waves/BACF22D84E12CE669AACFA08D49C686F.

[9] X. Barthelemy, M. L. Banner, W. L. Peirson, F. Fedele, M. Allis, and F. Dias. On a unified breaking onset threshold for gravity waves in deep and intermediate depth water. *Journal of Fluid Mechanics*, 841:463–488, Apr. 2018. ISSN 0022-1120, 1469-7645. doi: 10.1017/jfm.2018.93. URL https://www.cambridge.org/core/journals/journal-of-fluid-mechanics/article/on-a-unified-breaking-onset-threshold-for-gravity-waves-in-deep-and-intermediate-de
63A8E661999DEC94EB3B7BADC729DB0F.

[10] J. A. Battjes. Set-up Due to Irregular Waves. *Coastal Engineering Proceedings*, (13):109–109, Jan. 1972. ISSN 2156-1028. doi: 10.9753/icce.v13.109. URL https://icce-ojs-tamu.tdl.org/icce/article/view/2856. Number: 13.

[11] J. A. Battjes and J. P. F. M. Janssen. Energy Loss and Set-Up Due to Breaking of

Random Waves. In *Coastal Engineering 1978*, pages 569–587, Hamburg, Germany, Aug. 1978. American Society of Civil Engineers. ISBN 978-0-87262-190-9 978-0-7844-7960-5. doi: 10.1061/9780872621909.034. URL http://ascelibrary.org/doi/10.1061/9780872621909.034.

[12] P. S. Bell. Mapping shallow water coastal areas using a standard marine x-band radar. pages 4–1, Liverpool, 2008. URL https://nora.nerc.ac.uk/id/eprint/6476/. Num Pages: 9.

[13] F. Bergamasco, A. Torsello, M. Sclavo, F. Barbariol, and A. Benetazzo. WASS: An open-source pipeline for 3D stereo reconstruction of ocean waves. *Computers & Geosciences*, 107:28–36, Oct. 2017. ISSN 0098-3004. doi: 10.1016/j.cageo.2017.07.001. URL https://www.sciencedirect.com/science/article/pii/S0098300417304302. Read_Status: New Read_Status_Date: 2023-12-14T18:45:24.272Z.

[14] P. Bevandić, I. Krešo, M. Oršić, and S. Šegvić. Simultaneous Semantic Segmentation and Outlier Detection in Presence of Domain Shift, Aug. 2019. URL http://arxiv.org/abs/1908.01098. arXiv:1908.01098 [cs].

[15] W. Birkemeier and M. Forte. Field Research Facility: A User's Guide to the Survey Lines Dataset. Technical report, Engineer Research and Development Center (U.S.), Aug. 2019. URL https://hdl.handle.net/11681/33653.

[16] W. A. Birkemeier. Time Scales of Nearshore Profile Changes. *COASTAL ENGINEERING*, 1985.

[17] N. Booij. *Gravity waves on water with non-uniform depth and current.* PhD thesis, 1981. URL https://repository.tudelft.nl/file/File_cdd2e3c5-2478-4a7e-beb7-5ff2d5c4262f?preview=1.

[18] K. L. Brodie. ERDC/CHL MP-21-3 "Simultaneous mapping of coastal topogra-

phy and bathymetry from a lightweight multicamera UAS". Read_Status: New Read_Status_Date: 2023-12-14T18:45:24.270Z.

[19] B. L. Bruder and K. L. Brodie. CIRN Quantitative Coastal Imaging Toolbox. *SoftwareX*, 12:100582, July 2020. ISSN 23527110. doi: 10.1016/j.softx.2020.100582. URL https://linkinghub.elsevier.com/retrieve/pii/S2352711020302958.

[20] D. Buscombe and R. J. Carini. A Data-Driven Approach to Classifying Wave Breaking in Infrared Imagery. *Remote Sensing*, 11(7):859, Jan. 2019. ISSN 2072-4292. doi: 10.3390/rs11070859. URL https://www.mdpi.com/2072-4292/11/7/859. Publisher: Multidisciplinary Digital Publishing Institute.

[21] P. A. Catalan and M. C. Haller. Remote sensing of breaking wave phase speeds with application to non-linear depth inversions. *Coastal Engineering*, 55(1):93–111, Jan. 2008. ISSN 0378-3839. doi: 10.1016/j.coastaleng.2007.09.010. URL https://www.sciencedirect.com/science/article/pii/S0378383907001007.

[22] P. A. Catalan, M. C. Haller, R. A. Holman, and W. J. Plant. Optical and Microwave Detection of Wave Breaking in the Surf Zone. *IEEE Transactions on Geoscience and Remote Sensing*, 49(6):1879–1893, June 2011. ISSN 1558-0644. doi: 10.1109/TGRS.2010.2095864. URL https://ieeexplore.ieee.org/document/5682019. Conference Name: IEEE Transactions on Geoscience and Remote Sensing.

[23] L. Z.-H. Chuang, L.-C. Wu, Y.-D. Sun, and J.-W. Lai. Bathymetry Determination Based on Abundant Wavenumbers Estimated from the Local Phase Gradient of X-Band Radar Images. *Remote Sensing*, 13(21):4240, Jan. 2021. ISSN 2072-4292. doi: 10.3390/rs13214240. URL https://www.mdpi.com/2072-4292/13/21/4240. Publisher: Multidisciplinary Digital Publishing Institute.

[24] C. O. I. Collins and K. L. Brodie. In Situ Measurements of Directional Wave Spectra

from an Unmanned Aerial System. 2021. Read_Status: New Read_Status_Date: 2023-12-14T18:45:24.268Z.

[25] R. G. Dean. Equilibrium Beach Profiles: Characteristics and Applications. *Journal of Coastal Research*, 7(1):53–84, 1991. ISSN 0749-0208. URL https://www.jstor.org/stable/4297805. Publisher: Coastal Education & Research Foundation, Inc.

[26] A. Delić, M. Grcić, and S. Šegvić. Outlier detection by ensembling uncertainty with negative objectness, Sept. 2024. URL http://arxiv.org/abs/2402.15374. arXiv:2402.15374 [cs].

[27] Z. Demirbilek and C. L. Vincent. Coastal Engineering Manual - Part II. Technical Report EM_1110-2-1100, US Army Corps of Engineers, 2002. URL https://www.publications.usace.army.mil/USACE-Publications/Engineer-Manuals/u43544q/636F617374616C20656E67696E656572696E67206D616E75616C/.

[28] J. Deng, W. Dong, R. Socher, L.-J. Li, K. Li, and L. Fei-Fei. ImageNet: A large-scale hierarchical image database. In *2009 IEEE Conference on Computer Vision and Pattern Recognition*, pages 248–255, June 2009. doi: 10.1109/CVPR.2009.5206848. URL https://ieeexplore.ieee.org/document/5206848. ISSN: 1063-6919.

[29] M. Derakhti, J. T. Kirby, M. L. Banner, S. T. Grilli, and J. Thomson. A Unified Breaking Onset Criterion for Surface Gravity Water Waves in Arbitrary Depth. *Journal of Geophysical Research: Oceans*, 125(7): e2019JC015886, 2020. ISSN 2169-9291. doi: 10.1029/2019JC015886. URL https://onlinelibrary.wiley.com/doi/abs/10.1029/2019JC015886. _eprint: https://onlinelibrary.wiley.com/doi/pdf/10.1029/2019JC015886.

[30] F. J. Diez-Garias and M. Maia. U.S. Patent for Unmanned air and underwater vehicle Patent (Patent # 10,315,762 issued June 11, 2019) - Justia Patents Search, June 2019. URL https://patents.justia.com/patent/10315762.

[31] C. Eadi Stringari, P. Veras Guimarães, J.-F. Filipot, F. Leckler, and R. Duarte. Deep neural networks for active wave breaking classification. *Scientific Reports*, 11(1):3604, Feb. 2021. ISSN 2045-2322. doi: 10.1038/s41598-021-83188-y. URL https://www.nature.com/articles/s41598-021-83188-y. Publisher: Nature Publishing Group.

[32] M. Forte, W. Birkemeier, and J. R. Mitchell. Nearshore survey system evaluation. Technical report, Coastal and Hydraulics Laboratory (U.S.), Jan. 2018. URL http://hdl.handle.net/11681/26031.

[33] J. R. Gemmrich, M. L. Banner, and C. Garrett. Spectrally Resolved Energy Dissipation Rate and Momentum Flux of Breaking Waves. *Journal of Physical Oceanography*, 38 (6):1296–1312, June 2008. ISSN 1520-0485, 0022-3670. doi: 10.1175/2007JPO3762.1. URL http://journals.ametsoc.org/doi/10.1175/2007JPO3762.1.

[34] T. Halsne, A. Benetazzo, F. Barbariol, K. H. Christensen, A. Carrasco, and O. Breivik. Wave Modulation in a Strong Tidal Current and Its Impact on Extreme Waves. Dec. 2023. doi: 10.1175/JPO-D-23-0051.1. URL https://journals.ametsoc.org/view/journals/phoc/54/1/JPO-D-23-0051.1.xml. Section: Journal of Physical Oceanography.

[35] K. He, X. Zhang, S. Ren, and J. Sun. Deep Residual Learning for Image Recognition, Dec. 2015. URL http://arxiv.org/abs/1512.03385. arXiv:1512.03385 [cs].

[36] T. Hedges. TECHNICAL NOTE. AN EMPIRICAL MODIFICATION TO LINEAR WAVE THEORY. *Proceedings of the Institution of Civil Engineers*, 61(3):575–579, Sept. 1976. ISSN 1753-7789. doi: 10.1680/iicep.1976.3408. URL https://www.icevirtuallibrary.com/doi/10.1680/iicep.1976.3408.

[37] R. Holman and E. W. J. Bergsma. Updates to and Performance of the cBathy Algorithm for Estimating Nearshore Bathymetry from Remote Sensing Imagery. *Remote Sensing*, 13(19):3996, Jan. 2021. ISSN 2072-4292. doi: 10.3390/rs13193996. URL https://www.

mdpi.com/2072-4292/13/19/3996. Number: 19 Publisher: Multidisciplinary Digital Publishing Institute.

[38] R. Holman, N. Plant, and T. Holland. cBathy: A robust algorithm for estimating nearshore bathymetry. *Journal of Geophysical Research: Oceans*, 118(5):2595–2609, 2013. ISSN 2169-9291. doi: 10.1002/jgrc.20199. URL https://onlinelibrary.wiley.com/doi/abs/10.1002/jgrc.20199. _eprint: https://onlinelibrary.wiley.com/doi/pdf/10.1002/jgrc.20199 Read_Status: New Read_Status_Date: 2023-12-14T18:45:24.259Z.

[39] R. A. Holman and J. Stanley. The history and technical capabilities of Argus. *Coastal Engineering*, 54(6):477–491, June 2007. ISSN 0378-3839. doi: 10.1016/j.coastaleng.2007.01.003. URL https://www.sciencedirect.com/science/article/pii/S037838390700018X.

[40] R. A. Holman, K. L. Brodie, and N. J. Spore. Surf Zone Characterization Using a Small Quadcopter: Technical Issues and Procedures. *IEEE Transactions on Geoscience and Remote Sensing*, 55(4):2017–2027, Apr. 2017. ISSN 1558-0644. doi: 10.1109/TGRS.2016.2635120. URL https://ieeexplore.ieee.org/document/7809056. Conference Name: IEEE Transactions on Geoscience and Remote Sensing.

[41] D. L. Inman, R. J. Tait, and C. E. Nordstrom. Mixing in the surf zone. *Journal of Geophysical Research (1896-1977)*, 76(15):3493–3514, 1971. ISSN 2156-2202. doi: 10.1029/JC076i015p03493. URL https://onlinelibrary.wiley.com/doi/abs/10.1029/JC076i015p03493. _eprint: https://onlinelibrary.wiley.com/doi/pdf/10.1029/JC076i015p03493.

[42] J. T. Kirby and R. A. Dalrymple. An approximate model for nonlinear dispersion in monochromatic wave propagation models. *Coastal Engineering*, 9(6):545–561, Mar. 1986. ISSN 0378-3839. doi: 10.1016/0378-3839(86)90003-7. URL https://www.sciencedirect.com/science/article/pii/0378383986900037.

[43] A. N. Klotz, R. Almar, Y. Quenet, E. W. J. Bergsma, D. Youssefi, S. Artigues, N. Rascle, B. A. Sy, and A. Ndour. Nearshore satellite-derived bathymetry from a single-pass satellite video: Improvements from adaptive correlation window size and modulation transfer function. *Remote Sensing of Environment*, 315:114411, Dec. 2024. ISSN 0034-4257. doi: 10.1016/j.rse.2024.114411. URL https://www.sciencedirect.com/science/article/pii/S0034425724004371.

[44] A. M. Z. Lange, J. W. Fiedler, M. A. Merrifield, and R. T. Guza. UAV video-based estimates of nearshore bathymetry. *Coastal Engineering*, 185:104375, Oct. 2023. ISSN 0378-3839. doi: 10.1016/j.coastaleng.2023.104375. URL https://www.sciencedirect.com/science/article/pii/S0378383923000996.

[45] B. Le Mehaute. ON NON-SATURATED BREAKERS AND THE WAVE RUN-UP. *Coastal Engineering Proceedings*, (8):6, Jan. 1962. ISSN 2156-1028, 0589-087X. doi: 10.9753/icce.v8.6. URL https://icce-ojs-tamu.tdl.org/icce/article/view/2255.

[46] T.-Y. Lin, P. Goyal, R. Girshick, K. He, and P. Dollár. Focal Loss for Dense Object Detection, Feb. 2018. URL http://arxiv.org/abs/1708.02002. arXiv:1708.02002 [cs].

[47] T. C. Lippmann and R. A. Holman. Quantification of sand bar morphology: A video technique based on wave dissipation. *Journal of Geophysical Research: Oceans*, 94 (C1):995–1011, Jan. 1989. ISSN 0148-0227. doi: 10.1029/JC094iC01p00995. URL https://agupubs.onlinelibrary.wiley.com/doi/10.1029/JC094iC01p00995.

[48] I. Loshchilov and F. Hutter. Decoupled Weight Decay Regularization, Jan. 2019. URL http://arxiv.org/abs/1711.05101. arXiv:1711.05101 [cs].

[49] B. Lund, R. Carrasco, H. Dai, H. C. Graber, C. M. Guigand, B. K. Haus, J. Horstmann, J. A. Lodise, G. Novelli, T. Özgökmen, M. A. Rebozo, E. H. Ryan, and M. Streßer. UAS Current Mapping: A Wave-Based Heading and Position Correction. *Jour-*

nal of Atmospheric and Oceanic Technology, 38(9):1441–1455, Sept. 2021. ISSN 0739-0572, 1520-0426. doi: 10.1175/JTECH-D-20-0123.1. URL https://journals.ametsoc.org/view/journals/atot/38/9/JTECH-D-20-0123.1.xml. Read_Status: New Read_Status_Date: 2023-12-14T18:45:24.254Z.

[50] D. Lyzenga, N. Malinas, and F. Tanis. Multispectral bathymetry using a simple physically based algorithm. *IEEE Transactions on Geoscience and Remote Sensing*, 44 (8):2251–2259, Aug. 2006. ISSN 1558-0644. doi: 10.1109/TGRS.2006.872909. URL https://ieeexplore.ieee.org/document/1661813/.

[51] K. Martins, C. E. Blenkinsopp, and J. Zang. Monitoring Individual Wave Characteristics in the Inner Surf with a 2-Dimensional Laser Scanner (LiDAR). *Journal of Sensors*, 2016(1):7965431, 2016. ISSN 1687-7268. doi: 10.1155/2016/7965431. URL https://onlinelibrary.wiley.com/doi/abs/10.1155/2016/7965431. _eprint: https://onlinelibrary.wiley.com/doi/pdf/10.1155/2016/7965431.

[52] K. Martins, C. E. Blenkinsopp, R. Deigaard, and H. E. Power. Energy Dissipation in the Inner Surf Zone: New Insights From LiDAR-Based Roller Geometry Measurements. *Journal of Geophysical Research: Oceans*, 123(5):3386–3407, 2018. ISSN 2169-9291. doi: 10.1029/2017JC013369. URL https://onlinelibrary.wiley.com/doi/abs/10.1029/2017JC013369. _eprint: https://agupubs.onlinelibrary.wiley.com/doi/pdf/10.1029/2017JC013369.

[53] M. P. McCann, D. L. Anderson, C. R. Sherwood, B. Bruder, A. S. Bak, and K. L. Brodie. CoastalImageLib: An open- source Python package for creating common coastal image products. *SoftwareX*, 20:101215, Dec. 2022. ISSN 23527110. doi: 10.1016/j.softx.2022.101215. URL https://linkinghub.elsevier.com/retrieve/pii/S2352711022001339.

[54] G. Medellín, M. Mayor, C. M. Appendini, R. Cerezo-Mota, and J. A. Jiménez. The Role of Beach Morphology and Mid-Century Climate Change Effects on Wave Runup

and Storm Impact on the Northern Yucatan Coast. *Journal of Marine Science and Engineering*, 9(5):518, May 2021. ISSN 2077-1312. doi: 10.3390/jmse9050518. URL https://www.mdpi.com/2077-1312/9/5/518. Publisher: Multidisciplinary Digital Publishing Institute.

[55] M. Miche. Mouvements ondulatoires de la mer en profondeur constante ou décroissante. 1944. URL https://repository.tudelft.nl/record/uuid:6fceef55-d71b-4e3e-a94f-98ff17cb8f91.

[56] S. Moghimi, H. T. Özkan Haller, G. W. Wilson, and A. Kurapov. Data Assimilation for Bathymetry Estimation at a Tidal Inlet. *Journal of Atmospheric and Oceanic Technology*, 33(10):2145–2163, Oct. 2016. ISSN 0739-0572, 1520-0426. doi: 10.1175/JTECH-D-14-00188.1. URL https://journals.ametsoc.org/view/journals/atot/33/10/jtech-d-14-00188_1.xml. Read_Status: New Read_Status_Date: 2023-12-14T18:45:24.252Z.

[57] A. Morang and L. E. Parson. Coastal Engineering Manual - Part IV-1, Aug. 2008. URL https://www.publications.usace.army.mil/USACE-Publications/Engineer-Manuals/u43544q/636F617374616C20656E67696E656572696E67206D616E75616C/.

[58] M. A. Najar, R. Benshila, Y. E. Bennioui, G. Thoumyre, R. Almar, E. W. J. Bergsma, J.-M. Delvit, and D. G. Wilson. Coastal Bathymetry Estimation from Sentinel-2 Satellite Imagery: Comparing Deep Learning and Physics-Based Approaches. *Remote Sensing*, 14(5):1196, Jan. 2022. ISSN 2072-4292. doi: 10.3390/rs14051196. URL https://www.mdpi.com/2072-4292/14/5/1196. Publisher: Multidisciplinary Digital Publishing Institute.

[59] A. O'Dea, D. Anderson, R. Holman, C. Painter, and K. Brodie. Wave kinematics-based bathymetry estimates from satellite optical video. *Coastal Engineering*, 200:

104753, July 2025. ISSN 0378-3839. doi: 10.1016/j.coastaleng.2025.104753. URL https://www.sciencedirect.com/science/article/pii/S0378383925000584.

[60] M. Perlin, J. He, and L. P. Bernal. An experimental study of deep water plunging breakers. *Physics of Fluids*, 8(9):2365–2374, Sept. 1996. ISSN 1070-6631. doi: 10.1063/1.869021. URL https://doi.org/10.1063/1.869021.

[61] M. Perlin, W. Choi, and Z. Tian. Breaking Waves in Deep and Intermediate Waters. *Annual Review of Fluid Mechanics*, 45(1):115–145, Jan. 2013. ISSN 0066-4189, 1545-4479. doi: 10.1146/annurev-fluid-011212-140721. URL https://www.annualreviews.org/doi/10.1146/annurev-fluid-011212-140721.

[62] N. G. Plant, K. T. Holland, and J. A. Puleo. Analysis of the scale of errors in nearshore bathymetric data. *Marine Geology*, 191(1):71–86, Nov. 2002. ISSN 0025-3227. doi: 10.1016/S0025-3227(02)00497-8. URL https://www.sciencedirect.com/science/article/pii/S0025322702004978.

[63] N. G. Plant, K. T. Holland, and M. C. Haller. Ocean Wavenumber Estimation From Wave-Resolving Time Series Imagery. *IEEE Transactions on Geoscience and Remote Sensing*, 46(9):2644–2658, Sept. 2008. ISSN 1558-0644. doi: 10.1109/TGRS.2008.919821. URL https://ieeexplore.ieee.org/document/4599199.

[64] M. Postacchini and M. Brocchini. A wave-by-wave analysis for the evaluation of the breaking-wave celerity. *Applied Ocean Research*, 46:15–27, June 2014. ISSN 0141-1187. doi: 10.1016/j.apor.2014.01.005. URL https://www.sciencedirect.com/science/article/pii/S0141118714000078.

[65] B. Raubenheimer, R. T. Guza, and S. Elgar. Wave transformation across the inner surf zone. *Journal of Geophysical Research: Oceans*, 101(C11):25589–25597, Nov. 1996. ISSN 0148-0227. doi: 10.1029/96JC02433. URL https://agupubs.onlinelibrary.wiley.com/doi/10.1029/96JC02433.

[66] I. Robertson, A. Alvaro, S. Verma, B. Jones, J. Levy, M. Gokdepe, and Z. Huang. Quantifying the Impacts of Artificial Reef Structures on Breaking Waves Using Cross-Shore Imagery and Machine Learning. AGU, Dec. 2024. URL https://agu.confex.com/agu/agu24/meetingapp.cgi/Paper/1588849.

[67] O. Ronneberger, P. Fischer, and T. Brox. U-Net: Convolutional Networks for Biomedical Image Segmentation, May 2015. URL http://arxiv.org/abs/1505.04597. arXiv:1505.04597 [cs].

[68] B. G. Ruessink and A. Kroon. The behaviour of a multiple bar system in the nearshore zone of Terschelling, the Netherlands: 1965–1993. *Marine Geology*, 121(3):187–197, Nov. 1994. ISSN 0025-3227. doi: 10.1016/0025-3227(94)90030-2. URL https://www.sciencedirect.com/science/article/pii/0025322794900302.

[69] A. H. Sallenger Jr. and R. A. Holman. Wave energy saturation on a natural beach of variable slope. *Journal of Geophysical Research: Oceans*, 90(C6): 11939–11944, 1985. ISSN 2156-2202. doi: 10.1029/JC090iC06p11939. URL https://onlinelibrary.wiley.com/doi/abs/10.1029/JC090iC06p11939. _eprint: https://agupubs.onlinelibrary.wiley.com/doi/pdf/10.1029/JC090iC06p11939.

[70] B. Sekachev, N. Manovich, M. Zhiltsov, A. Zhavoronkov, D. Kalinin, B. Hoff, TOsmanov, D. Kruchinin, A. Zankevich, DmitriySidnev, M. Markelov, Johannes222, M. Chenuet, a-andre, telenachos, A. Melnikov, J. Kim, L. Ilouz, N. Glazov, Priya4607, R. Tehrani, S. Jeong, V. Skubriev, S. Yonekura, v. truong, zliang7, lizhming, and T. Truong. opencv/cvat: v1.1.0, Aug. 2020. URL https://doi.org/10.5281/zenodo.4009388.

[71] G. Simarro and D. Calvete. UBathy (v2.0): A Software to Obtain the Bathymetry from Video Imagery. *Remote Sensing*, 14(23):6139, Jan. 2022. ISSN 2072-4292. doi: 10.3390/rs14236139. URL https://www.mdpi.com/2072-4292/14/23/6139. Number: 23 Publisher: Multidisciplinary Digital Publishing Institute.

[72] L. N. Smith and N. Topin. Super-Convergence: Very Fast Training of Neural Networks Using Large Learning Rates, May 2018. URL http://arxiv.org/abs/1708.07120. arXiv:1708.07120 [cs].

[73] M. Streser, R. Carrasco, and J. Horstmann. Video-Based Estimation of Surface Currents Using a Low-Cost Quadcopter. *IEEE Geoscience and Remote Sensing Letters*, 14 (11):2027–2031, Nov. 2017. ISSN 1545-598X, 1558-0571. doi: 10.1109/LGRS.2017.2749120. URL http://ieeexplore.ieee.org/document/8049342/. Read_Status: New Read_Status_Date: 2023-12-14T18:45:24.244Z.

[74] C. E. Stringari and H. E. Power. The Fraction of Broken Waves in Natural Surf Zones. *Journal of Geophysical Research: Oceans*, 124(12): 9114–9140, 2019. ISSN 2169-9291. doi: 10.1029/2019JC015213. URL https://onlinelibrary.wiley.com/doi/abs/10.1029/2019JC015213. _eprint: https://onlinelibrary.wiley.com/doi/pdf/10.1029/2019JC015213.

[75] C. E. Stringari and H. E. Power. Quantifying Bore-Bore Capture on Natural Beaches. *Journal of Geophysical Research: Oceans*, 125(6): e2019JC015689, 2020. ISSN 2169-9291. doi: 10.1029/2019JC015689. URL https://onlinelibrary.wiley.com/doi/abs/10.1029/2019JC015689. _eprint: https://onlinelibrary.wiley.com/doi/pdf/10.1029/2019JC015689.

[76] C. E. Stringari, D. L. Harris, and H. E. Power. A novel machine learning algorithm for tracking remotely sensed waves in the surf zone. *Coastal Engineering*, 147:149–158, May 2019. ISSN 0378-3839. doi: 10.1016/j.coastaleng.2019.02.002. URL https://www.sciencedirect.com/science/article/pii/S037838391830228X.

[77] R. P. Stumpf, K. Holderied, and M. Sinclair. Determination of water depth with high-resolution satellite imagery over variable bottom types. *Limnology and Oceanography*, 48(1part2):547–556, 2003. ISSN 1939-5590. doi: 10.4319/lo.2003.48.1_part_2.0547. URL https://

onlinelibrary.wiley.com/doi/abs/10.4319/lo.2003.48.1_part_2.0547. _eprint: https://aslopubs.onlinelibrary.wiley.com/doi/pdf/10.4319/lo.2003.48.1_part_2.0547.

[78] C. H. Sudre, W. Li, T. Vercauteren, S. Ourselin, and M. J. Cardoso. Generalised Dice overlap as a deep learning loss function for highly unbalanced segmentations. volume 10553, pages 240–248. 2017. doi: 10.1007/978-3-319-67558-9_28. URL http://arxiv.org/abs/1707.03237. arXiv:1707.03237 [cs].

[79] I. A. Svendsen. *Introduction to Nearshore Hydrodynamics*. World Scientific, 2006. ISBN 978-981-256-142-8.

[80] I. A. Svendsen, P. A. Madsen, and J. B. Hansen. Wave Characteristics in the Surf Zone. In *Coastal Engineering 1978*, pages 520–539, Hamburg, Germany, Aug. 1978. American Society of Civil Engineers. ISBN 978-0-87262-190-9 978-0-7844-7960-5. doi: 10.1061/9780872621909.031. URL http://ascelibrary.org/doi/10.1061/9780872621909.031.

[81] F. J. Sáez, P. A. Catalán, and C. Valle. Wave-by-wave nearshore wave breaking identification using U-Net. *Coastal Engineering*, 170:104021, Dec. 2021. ISSN 0378-3839. doi: 10.1016/j.coastaleng.2021.104021. URL https://www.sciencedirect.com/science/article/pii/S037838392100168X.

[82] E. B. Thornton and R. T. Guza. Energy saturation and phase speeds measured on a natural beach. *Journal of Geophysical Research: Oceans*, 87(C12):9499–9508, Nov. 1982. ISSN 0148-0227. doi: 10.1029/JC087iC12p09499. URL https://agupubs.onlinelibrary.wiley.com/doi/10.1029/JC087iC12p09499.

[83] E. B. Thornton and R. T. Guza. Transformation of wave height distribution. *Journal of Geophysical Research: Oceans*, 88(C10):5925–5938, July 1983. ISSN 0148-0227. doi: 10.1029/JC088iC10p05925. URL https://agupubs.onlinelibrary.wiley.com/doi/10.1029/JC088iC10p05925.

[84] K. Todd Holland. Beach cusp formation and spacings at Duck, USA. *Continental Shelf Research*, 18(10):1081–1098, Aug. 1998. ISSN 0278-4343. doi: 10.1016/S0278-4343(98)00024-7. URL https://www.sciencedirect.com/science/article/pii/S0278434398000247.

[85] N. Usuyama. pytorch-unet: Simple PyTorch implementations of U-Net/FullyConvNet (FCN) for image segmentation. URL https://github.com/usuyama/pytorch-unet/tree/master.

[86] A. van Dongeren, N. Plant, A. Cohen, D. Roelvink, M. C. Haller, and P. Catalán. Beach Wizard: Nearshore bathymetry estimation through assimilation of model computations and remote observations. *Coastal Engineering*, 55(12):1016–1027, Dec. 2008. ISSN 0378-3839. doi: 10.1016/j.coastaleng.2008.04.011. URL https://www.sciencedirect.com/science/article/pii/S0378383908000884.

[87] G. Vieira da Silva, D. Strauss, T. Murray, F. Alvarez, M. Hemer, A. Meucci, and O. Repina. Longshore Sediment Transport and Morphological Changes Under Climate Change—A Comparison Between CMIP5- and CMIP6-Derived Forcings and the Use of Wave Climate Bias Correction. *Journal of Geophysical Research: Oceans*, 130(6):e2024JC022212, 2025. ISSN 2169-9291. doi: 10.1029/2024JC022212. URL https://onlinelibrary.wiley.com/doi/abs/10.1029/2024JC022212. _eprint: https://agupubs.onlinelibrary.wiley.com/doi/pdf/10.1029/2024JC022212.

[88] J. R. Walker. Refraction of Finite-Height and Breaking Waves. pages 507–524, Jan. 1976. doi: 10.1061/9780872620834.029. URL https://ascelibrary.org/doi/10.1061/9780872620834.029. Publisher: American Society of Civil Engineers.

[89] R. E. Walker. *Marine light field statistics*. Wiley, New York, 1994. ISBN 978-0-471-31046-4. Open Library ID: OL1433582M.

[90] W. W. Williams. The Determination of Gradients on Enemy-Held Beaches. *The Geo-*

graphical Journal, 109(1/3):76–90, 1947. ISSN 0016-7398. doi: 10.2307/1789903. URL https://www.jstor.org/stable/1789903. Publisher: [Wiley, Royal Geographical Society (with the Institute of British Geographers)].

[91] G. Wilson and H. T. Özkan Haller. Ensemble-Based Data Assimilation for Estimation of River Depths. Oct. 2012. doi: 10.1175/JTECH-D-12-00014.1. URL https://journals.ametsoc.org/view/journals/atot/29/10/jtech-d-12-00014_1.xml. Section: Journal of Atmospheric and Oceanic Technology.

[92] G. W. Wilson, H. T. Özkan Haller, and R. A. Holman. Data assimilation and bathymetric inversion in a two-dimensional horizontal surf zone model. *Journal of Geophysical Research: Oceans*, 115(C12), 2010. ISSN 2156-2202. doi: 10.1029/2010JC006286. URL https://onlinelibrary.wiley.com/doi/abs/10.1029/2010JC006286. _eprint: https://onlinelibrary.wiley.com/doi/pdf/10.1029/2010JC006286 Read_Status: New Read_Status_Date: 2023-12-14T18:45:24.239Z.

[93] J. Wu, X. Hao, T. Li, and L. Shen. Adjoint-based high-order spectral method of wave simulation for coastal bathymetry reconstruction. *Journal of Fluid Mechanics*, 972: A41, Oct. 2023. ISSN 0022-1120, 1469-7645. doi: 10.1017/jfm.2023.733. URL https://www.cambridge.org/core/journals/journal-of-fluid-mechanics/article/adjointbased-highorder-spectral-method-of-wave-simulation-for-coastal-bathymetry-re
B53877DB9A4C96F3A2695B4F18F49EA7#sec3. Publisher: Cambridge University Press.

[94] J. Yoo, H. M. Fritz, K. A. Haas, P. A. Work, and C. F. Barnes. Depth Inversion in the Surf Zone with Inclusion of Wave Nonlinearity Using Video-Derived Celerity. *Journal of Waterway, Port, Coastal, and Ocean Engineering*, 137(2):95–106, Mar. 2011. ISSN 0733-950X, 1943-5460. doi: 10.1061/(ASCE)WW.1943-5460.0000068. URL https://ascelibrary.org/doi/10.1061/%28ASCE%29WW.1943-5460.0000068.

[95] S. J. Zaroodny. McCowan's Solitary Wave Expansions.